DTU Library

Monitoring oxygen production on mass-selected iridium–tantalum oxide electrocatalysts

Zheng, Ya-Rong; Vernieres, Jerome; Wang, Zhenbin; Zhang, Ke; Hochfilzer, Degenhart; Krempl, Kevin; Liao, Ting-Wei; Presel, Francesco; Altantzis, Thomas; Fatermans, Jarmo

Total number of authors:
21

Link back to DTU Orbit

Supplementary Information

Monitoring Oxygen Production on Mass-Selected Iridium-Tantalum Oxide Electrocatalysts

Zheng et al.
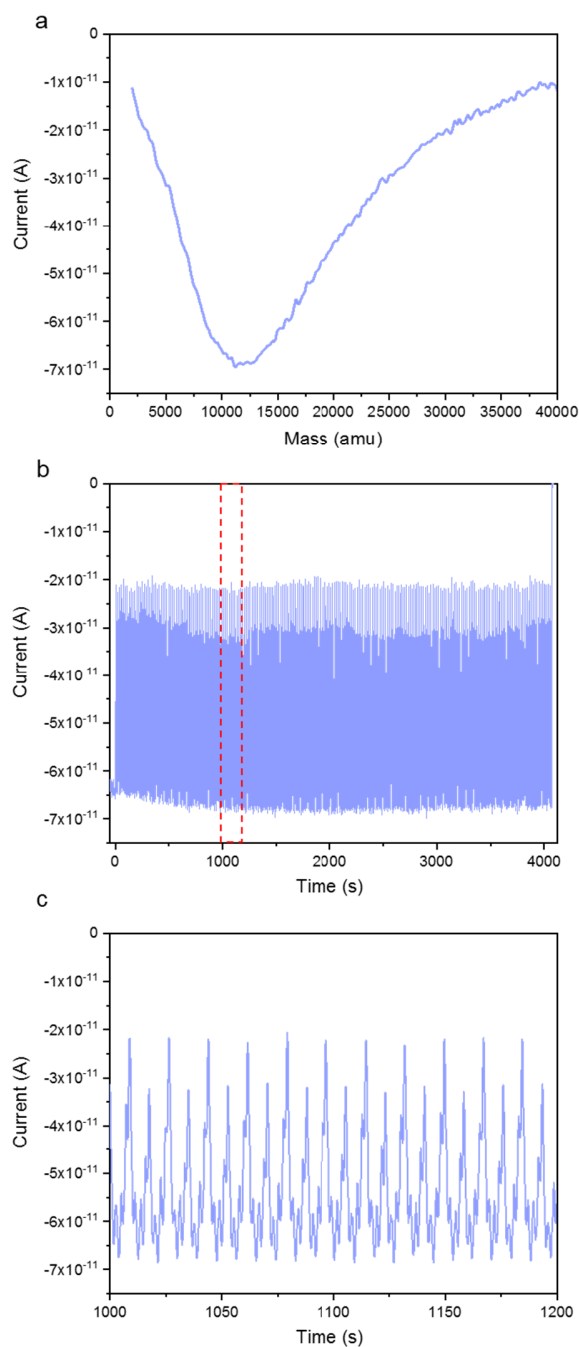
Supplementary Figure 1. Cluster deposition of 1.2×10^4 amu Ir-Ta particles. a, Mass spectrum of Ir-Ta particles with optimized deposition parameters. **b,** Cluster deposition of 5% coverage of 1.2×10^4 amu Ir-Ta particles on Au support with a geometric area of 0.196 cm². **c,** 200 s deposition of 1.2×10^4 amu Ir-Ta in (b). The changing deposition current was due to the applied raster amplitude in front of the beam to realize a homogeneous deposition on the support[1].

a

b

c

10 nm

5 nm

5 nm

d

e

f

10 nm

5 nm

5 nm
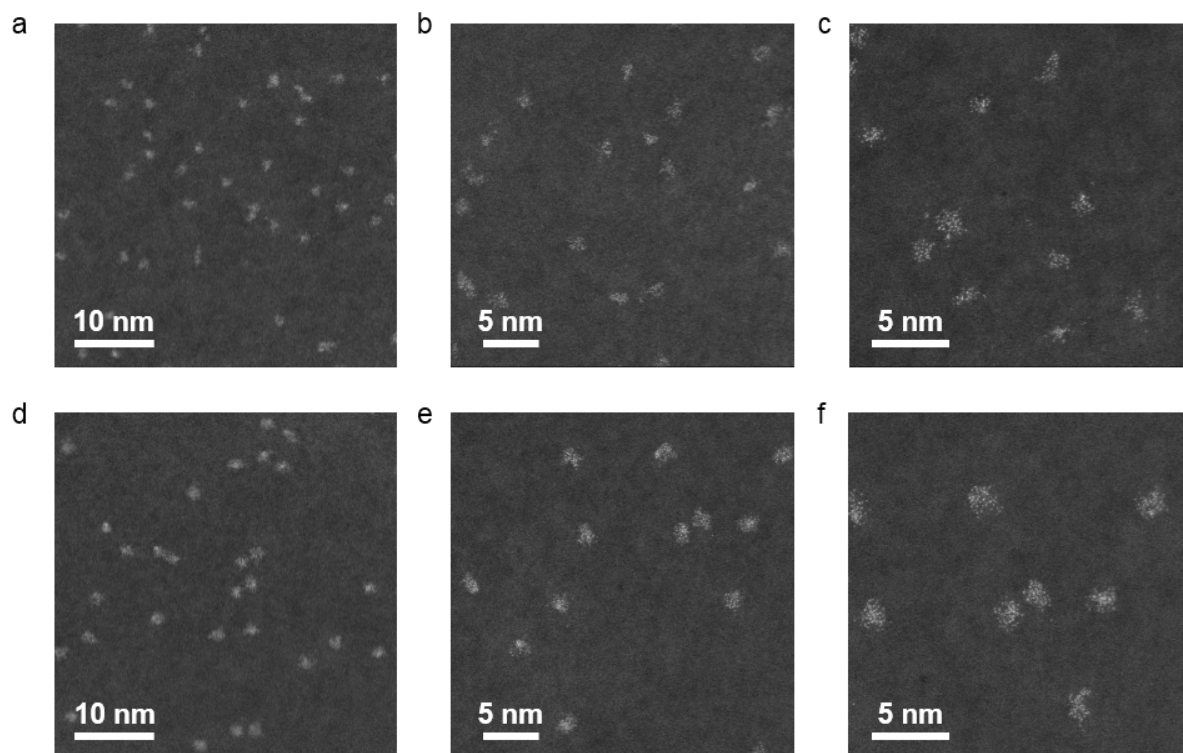
Supplementary Figure 2. ADF-STEM images of mass-selected (**a-c**) 6.0×10^3 and (**d-f**) 1.2×10^4 amu Ir-Ta particles after exposure in air. For each sample, overview images from 29 different regions were acquired and the results were similar.
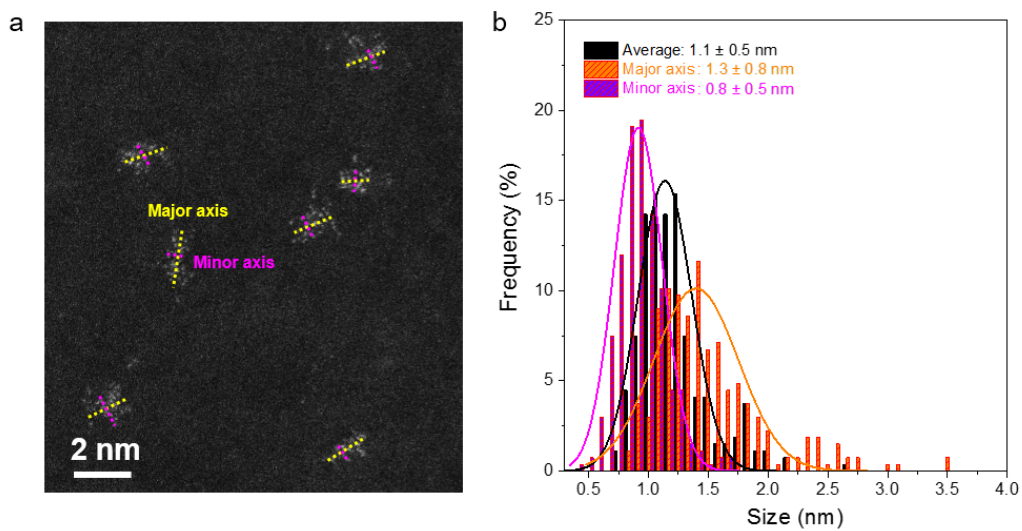
Supplementary Figure 3. Size distribution analysis of 1.2×10^4 amu Ir-Ta particles after exposure to air. Due to the irregular morphology of small size particles, the size of each particle was investigated by averaging the major axis and minor axis. 282 particles of 1.2×10^4 amu Ir-Ta were studied to obtain the size distribution.
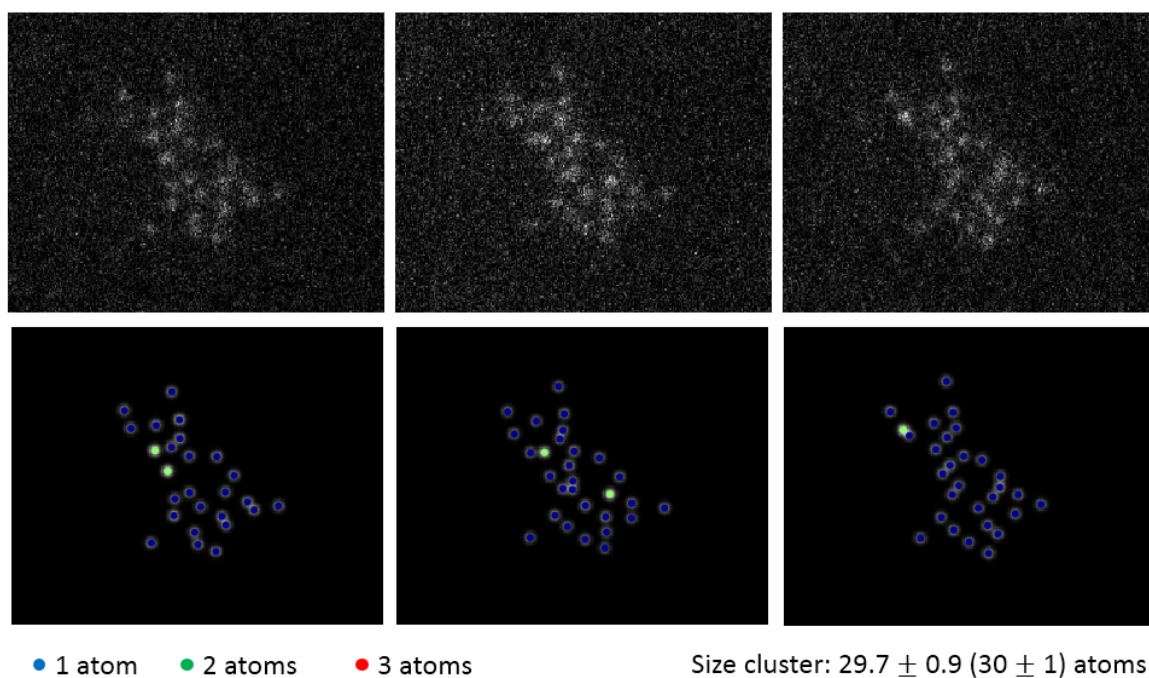
Supplementary Figure 4. Three consecutive frames of one 6.0×10^3 amu Ir-Ta particle from an ADF-STEM time series. The size of the cluster has been estimated to be 30 ± 1 atoms by averaging the atom-counting results throughout the three frames. Quantification of the Ir-Ta particle sizes from the high-resolution ADF-STEM images has been performed by using the freely available StatSTEM software[2], which allows to model the atomic columns in the image as two-dimensional Gaussian peaks. As such, the total amount of intensities scattered by an atomic column, the so-called scattering cross-section, has been estimated for each column. By applying a statistical atom-counting method[3,4], available within StatSTEM, the scattering cross-section of an atom column has been related to the amount of atoms present in the column. Therefore, the total size of the Ir-Ta particles could be determined.

● 1 atom   ● 2 atoms
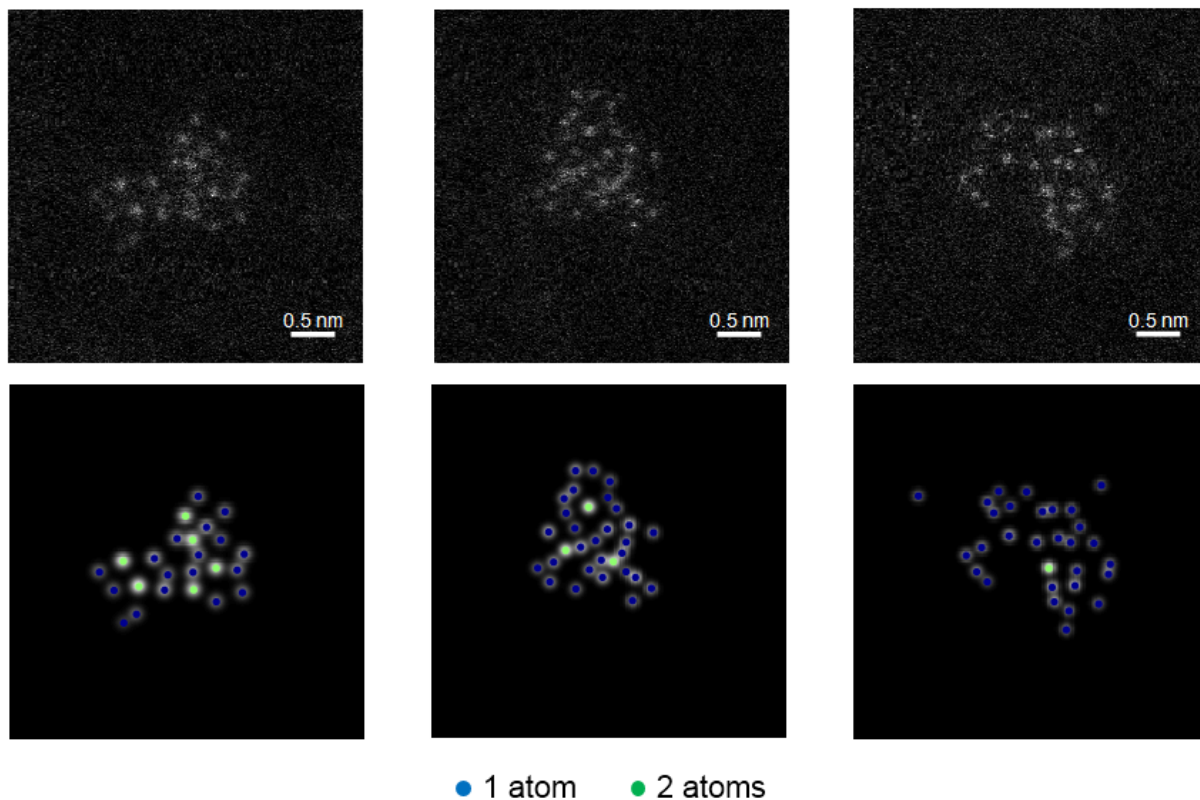
Supplementary Figure 5. Atom-counting results of three different 6.0×10^3 amu Ir-Ta particles. The particle size of 31 ± 2 atoms was obtained by analyzing 12 different particles.
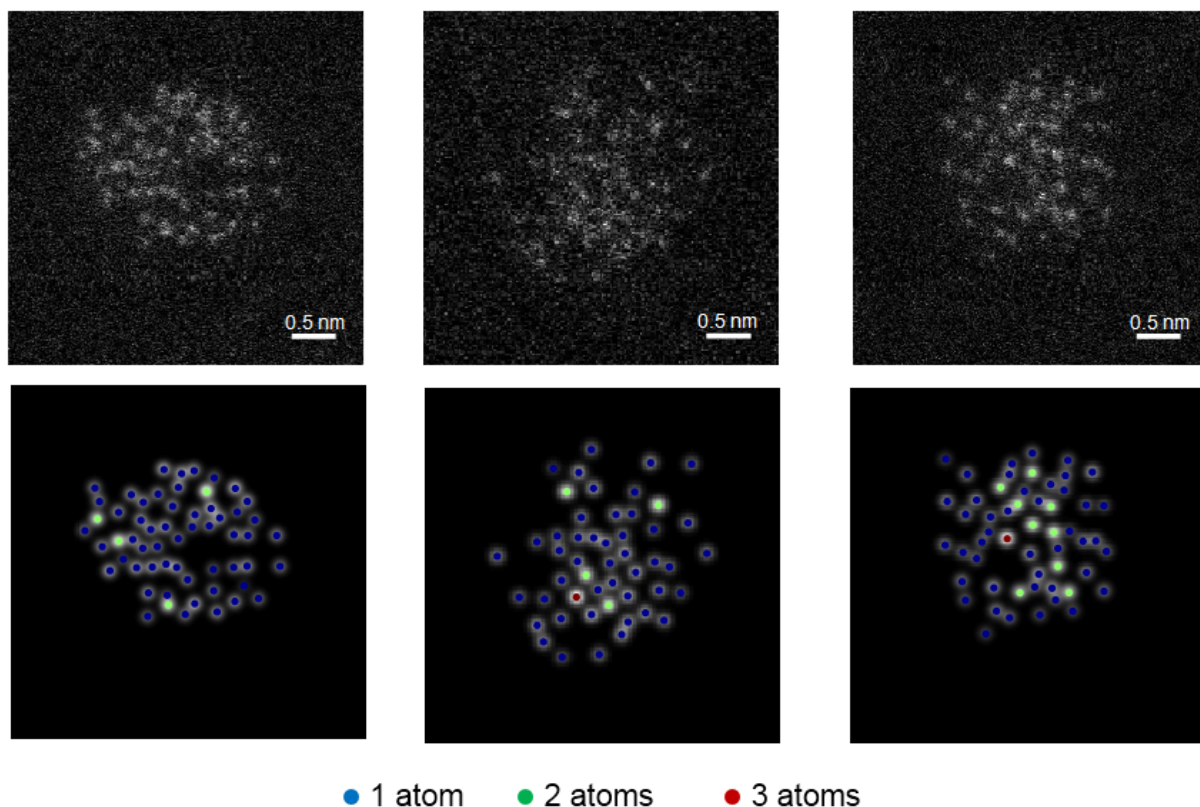
Supplementary Figure 6. Atom-counting results of three different 1.2×10^4 amu Ir-Ta particles. The particle size of 67 ± 6 atoms was obtained by analyzing 26 different particles.
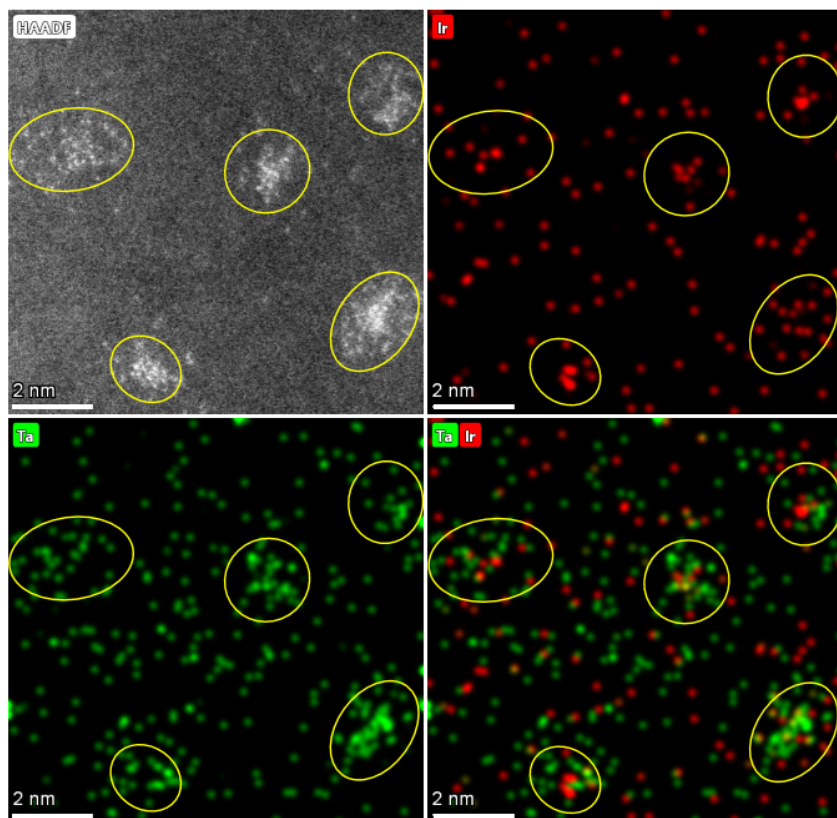
Supplementary Figure 7. STEM-EDS mapping of as-prepared 1.2×10^4 amu Ir-Ta particles after exposure to air.
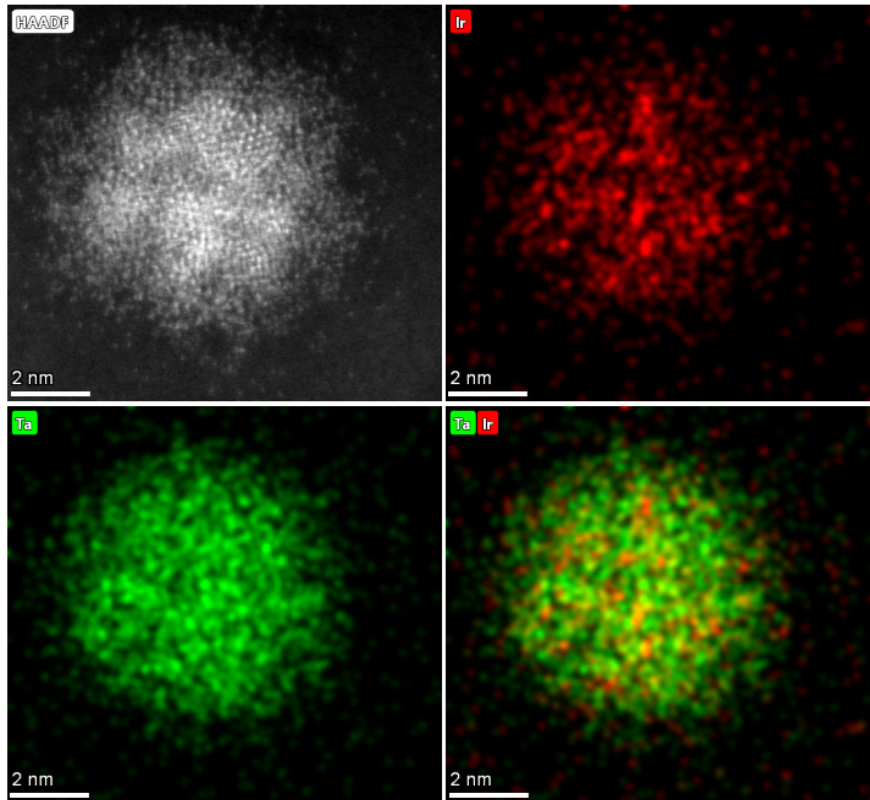
Supplementary Figure 8. STEM-EDS mapping of as-prepared 6.0×10^5 amu Ir-Ta particles after exposure to air.
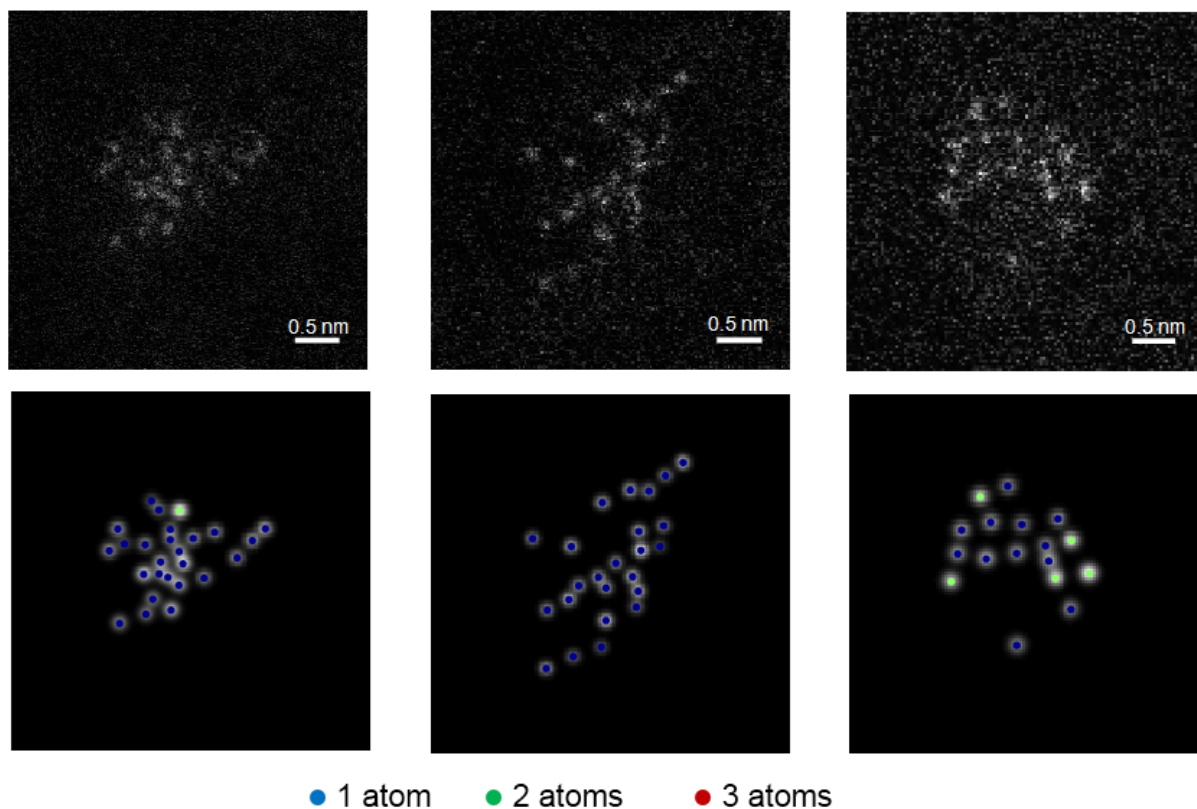
Supplementary Figure 9. Atom-counting results of three different 6.0×10^3 amu Ir-Ta particles after oxidation at 400 °C in air for 1 min. The particle size of 27 ± 4 atoms was obtained by analyzing 13 different particles. The oxidation process doesn't change the morphology of the particles, and most atoms of a particle are exposed on the surface without many overlap.

● 1 atom ● 2 atoms ● 3 atoms
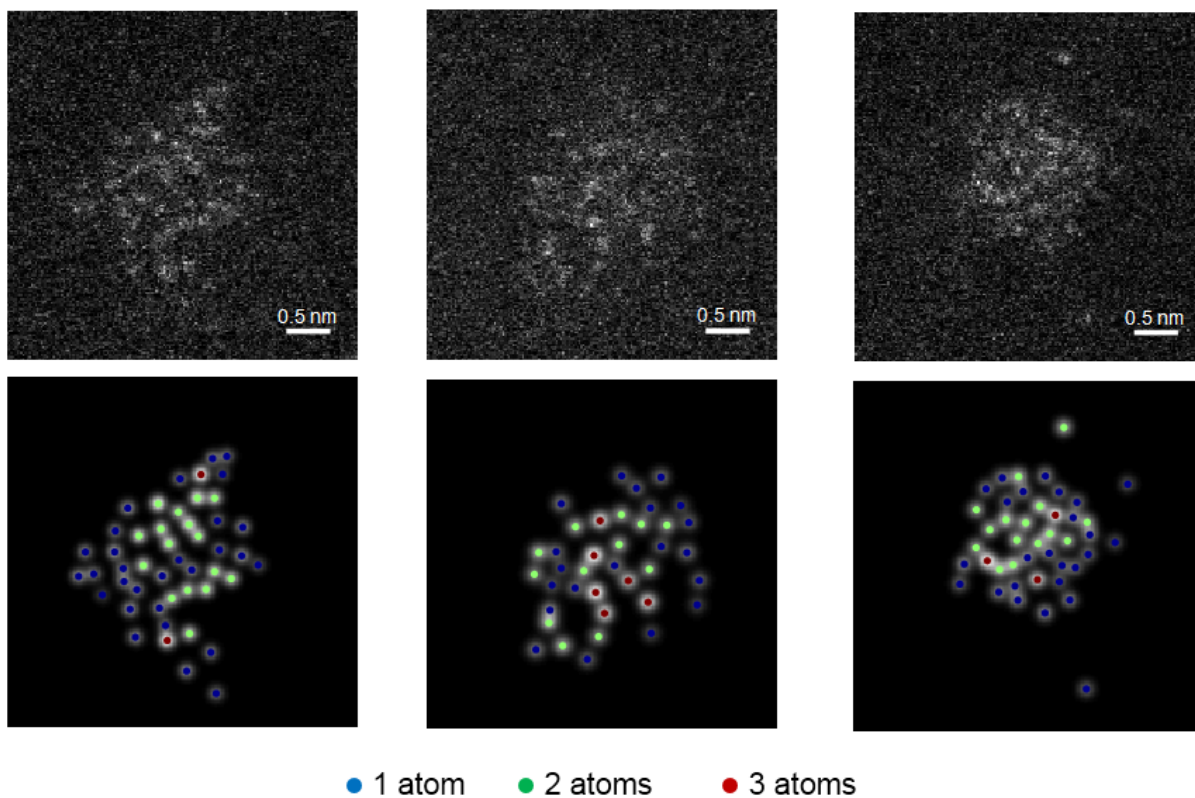
Supplementary Figure 10. Atom-counting results of three different 1.2×10^4 amu Ir-Ta particles after oxidation at 400 °C in air for 1 min. The particle size of 67 ± 6 atoms was obtained by analyzing 6 different particles.
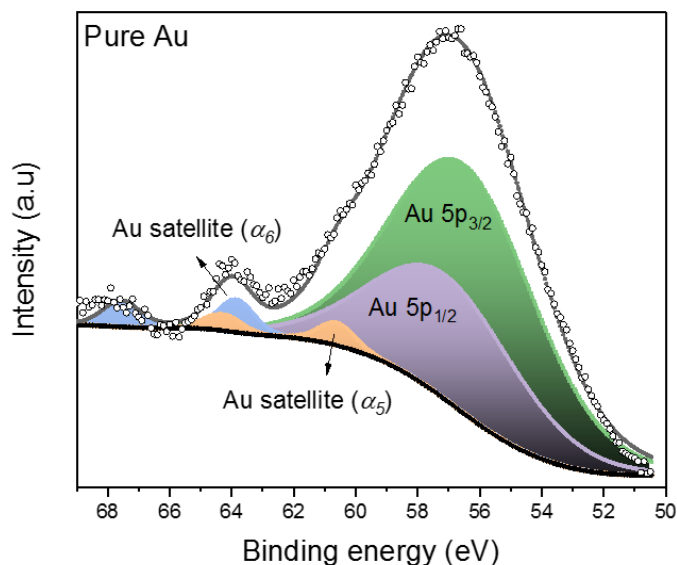
Supplementary Figure 11. XPS spectrum of the Au 5p in Ir 4f region for pure Au electrode. The Au 5p/Ir 4f core-level region for the clean electrode could not be fitted by a single set of peaks (Au $5p_{3/2}$ and Au $5p_{1/2}$), which suggests that additional features are present in this region. These additional features are X-ray satellites in which their intensities and spacing are characteristic of the X-ray anode material (Al Kα source) (ref.[5]). The α_5 and α_6 satellites are fitted with two doublets located at a binding energies of 60.6 eV and 63.9 eV, respectively. The energy splitting is kept similar to the Au 4f doublet (ΔE is around 3.67 eV) and the relative height is equal to 0.4% (α_5) and 0.3% (α_6) of the Au 4f 7/2 peak height. The atomic concentrations were quantified by integration of the Ta 4f and Ir 4f peaks after background subtraction. A Shirley-type background and a combination of Gaussian and Lorentzian fitting functions were chosen for this purpose (see in main text Fig. 1f). However, as it can be seen from Fig. S11, the Au 5p in Ir 4f region before nanoparticle deposition, demonstrates a strong overlap of the Au 5p in that region hindering an accurate quantification of the Ir 4f signal without data processing. In order to accurately extract the Ir 4f signal from this acquired region, we used a processing tool called "Spectrum calculator" (CasaXPS software). This function allows to perform basic arithmetic operations (addition, subtraction, *etc*.) between regions of interest acquired at different steps of the study (*e.g.* comparing spectra before and after the deposition, oxidation or OER activity test). The resulting spectral data are then used as part of the quantification procedure.
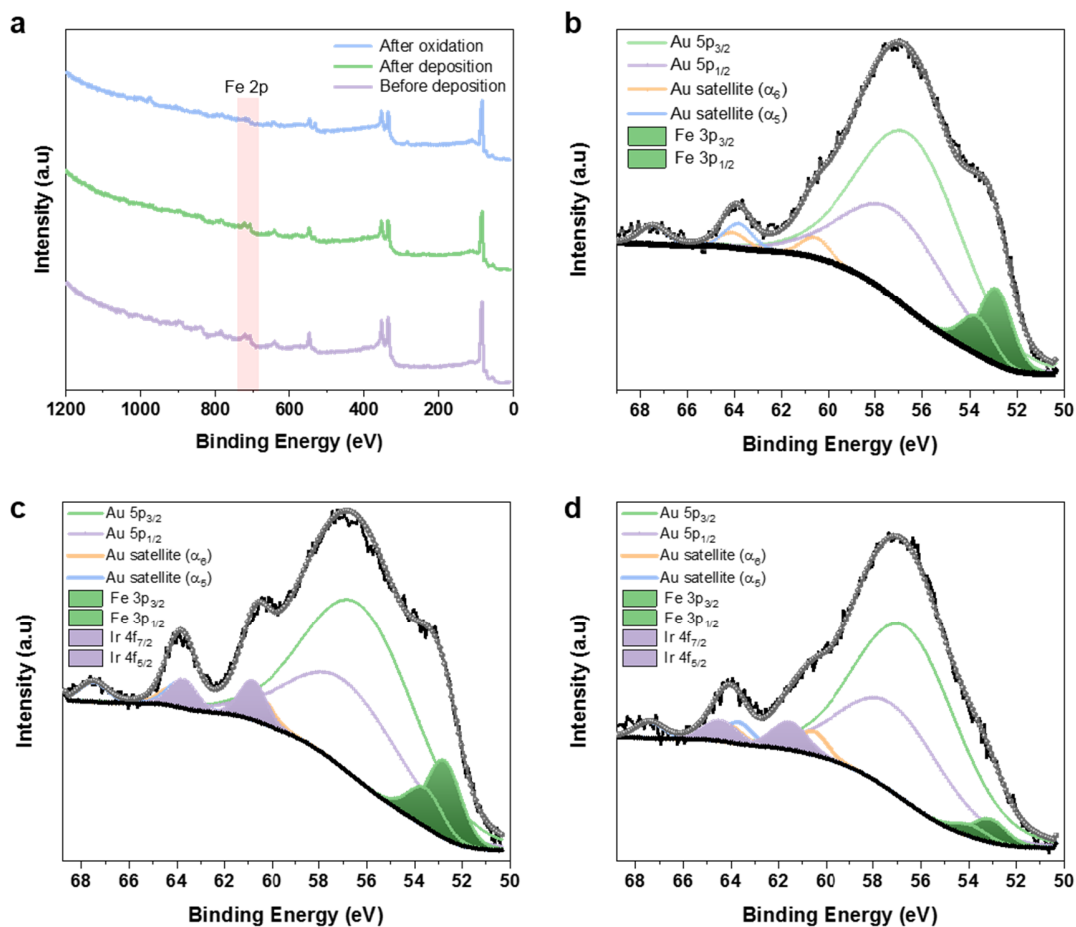
Supplementary Figure 12. XPS survey spectra (a) and Ir 4f/Au 5p region spectra for before (b) and after nanoparticles deposition (c), and after oxidation (d), respectively. Data processing have been performed to extract the Ir 4f signal due to the strongly overlapping Au 5p and Au satellites within this region, as shown in the Supplementary Figure 11. In addition, we provide in Supplementary Figure 12 a complete deconvolution of each elements within this region for each step of the process (before and after nanoparticles deposition, and after oxidation). The deconvolution of each Au components (5p and satellites) within this region are done in a similar manner as previously explained in Supplementary Figure 11 (*e.g,* their relative height are kept at 0.4% (α_5) and 0.3% (α_6) of their corresponding Au 4f 7/2 peak height). Both methods gave similar atomic composition between Ta and Ir. However, for a clearer visibility of the Ir 4f contribution, we show only the Ir4f signal after data processing in the main manuscript. Moreover, the survey spectra shown in the Supplementary Figure 12 reveals a contribution of Fe (Fe 2p), which is attributed to our sample holder. To maximize the signal over noise ratio we used a fairly large spot size, which explains why in most cases this Fe contribution appears, although sometimes this contribution is weaker or almost inexistant (see Supplementary Figure 11 or the spectra after oxidation in Supplementary Figure 12).
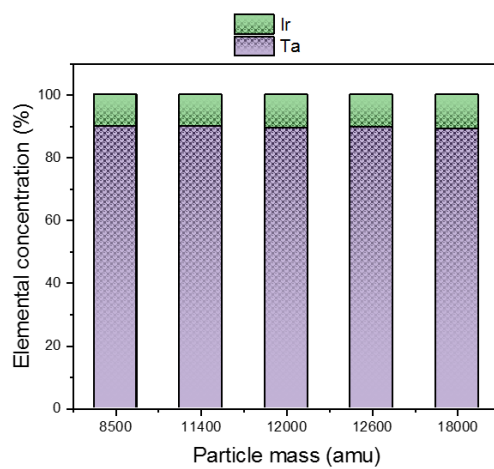
Supplementary Figure 13. XPS quantification of the elemental compositions of mass-selected $Ir_{0.1}Ta_{0.9}O_{2.45}$ particles with different masses.
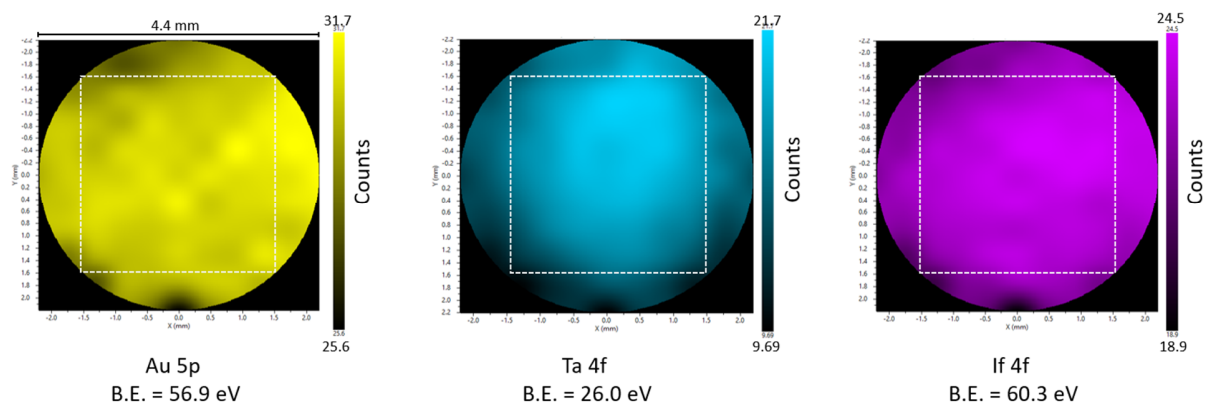
Supplementary Figure 14. XPS elemental imaging of 5% coverage 1.2×10⁴ amu IrTa₉ NPs on Au support. Here, the diameter of the Au disk is 5 mm, the XPS spectra of Au 5p, Ta 4f, and Ir 4f were taken within a 4.4 mm circular. The XPS imaging clearly shows a uniform spatial distribution of Ta and If throughout the detected region of the prepared 1.2×10⁴ amu IrTa₉ NPs on Au support.
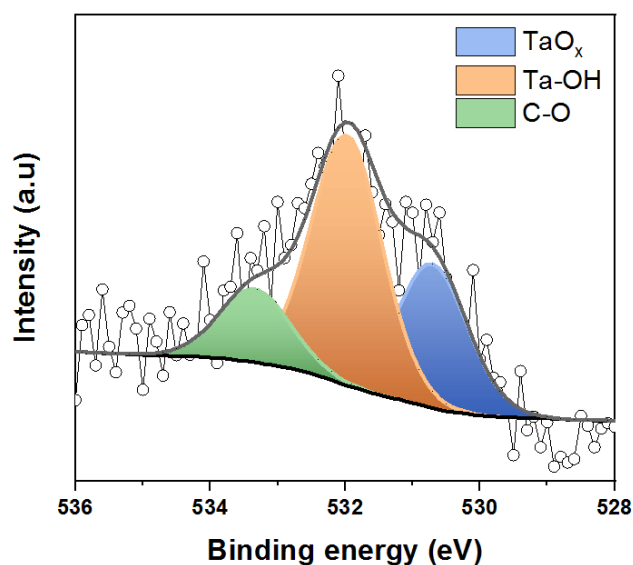
Supplementary Figure 15. XPS spectrum of the O 1s of 1.2×10^4 amu as-deposited sample cleaned before and after deposition. A peak at 530.6 eV (blue) can be observed and it is often attributed to the O^{2-} anions of the crystalline network[6]. In our case, this peak is attributed to Ta oxide. Besides this peak, another intense peak can be observed at a binding energy of 531.9 eV (orange). The adsorption of OH^- group has been suggested at this binding energy range[6], although these features are not precisely attributed in the literature. Finally, a weaker peak at a higher binding energy of 533.2 eV (green) is observed and can be attributed to carbonic oxide[7].
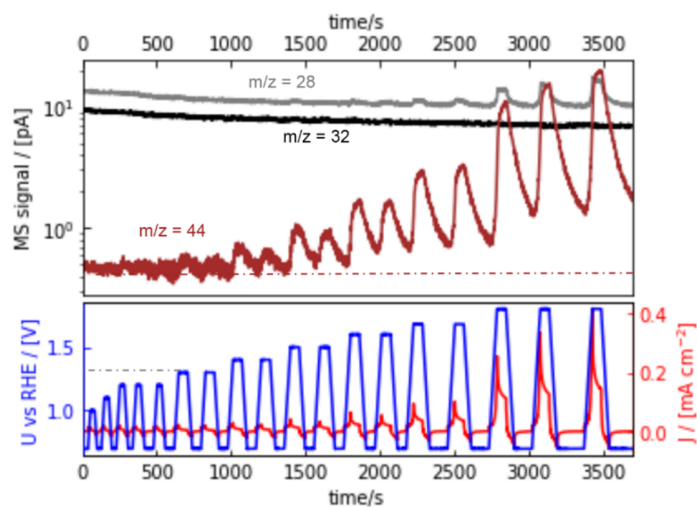
Supplementary Figure 16. EC-MS raw data of pure glassy carbon electrode in 0.1 M HClO$_4$. Bottom panel: Electrochemical potential cycling of pure glassy carbon electrode between open-circuit potential (OCP) and anodic potentials (1.0 to 1.9 V vs. RHE) at a scan rate of 20 mV s^{-1}. Electrolyte: 0.1 M HClO$_4$. Upper panel: Mass spectrometer signals for N$_2$/CO (*m/z* = 28, gray), O$_2$ (*m/z* = 32, black), and CO$_2$ (*m/z* = 44, red). As can be seen, the formation of CO$_2$ (*m/z* = 44) on glassy carbon is pronouncing when the anodic potential is higher than 1.4 eV, which is due to the carbon decomposition. The CO$_2$ production increases as the most anodic potential becomes more positive, and without any O$_2$ production. Carbon-based materials are commonly used as the supports for electrochemical measurements. However, the decomposition of carbon at high anodic potential range could severely affect the catalyst stability. Moreover, the carbon oxidation current might result in overestimating the actual OER performance.
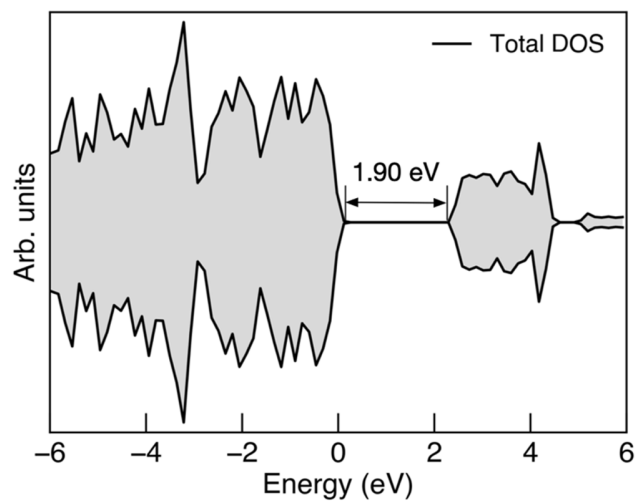
Supplementary Figure 17. Calculated density of State (DOS) of Au_2O_3 using the hybrid functional Heyd-Scuseria-Ernzerhof (HSE) (ref. 8).
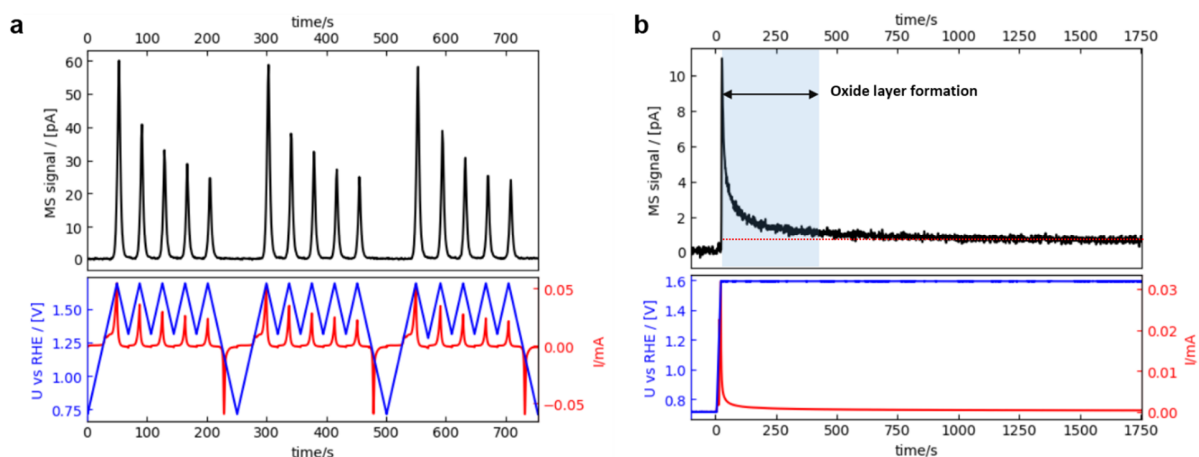
Supplementary Figure 18. EC-MS measurement of Au supported 1.32×10^4 amu $Ir_{0.1}Ta_{0.9}O_{2.45}$ NPs. a, Data was measured using cyclic voltammetry (CV) in 0.1 M HClO$_4$ at a scan rate 20 mV s^{-1} in 0.1 M HClO$_4$. **b,** Electrochemical chronoamperometric responses recorded on gold supported 1.32×10^4 amu $Ir_{0.1}Ta_{0.9}O_{2.45}$ at a constant potential of 1.6 V vs. RHE. Bottom panel: Electrochemical potential and current. Top panel: mass spectrometer signal for O$_2$. As shown in Supplementary Fig. 18a, the measurement was started at the OCP (~0.75 V vs. RHE), after the first cycle, the potential range was constrained between 1.3 ~ 1.7 V vs. RHE. One can see that, both MS O$_2$ signal and electrochemical current are dramatically decreased as more cycles, which is attributed to the oxide layer growing on gold electrode. The formation of gold surface (hydr)oixeds starts at *ca.* 1.3 V and could be further grown to a mixture of AuO and Au$_2$O$_3$ above 1.5 V vs. RHE (ref. [9]). After five cycles, the potential was swept back to the initial OCP value of 0.75 V vs. RHE, and the oxidized Au surface could be reduced at *ca.* 1.2 V vs. RHE. Supplementary Fig. 18b reveals that the thicker oxide film could be formed within 5 min at 1.6 V vs. RHE. The OER activity could be recovered after reducing the gold electrode at OCP.
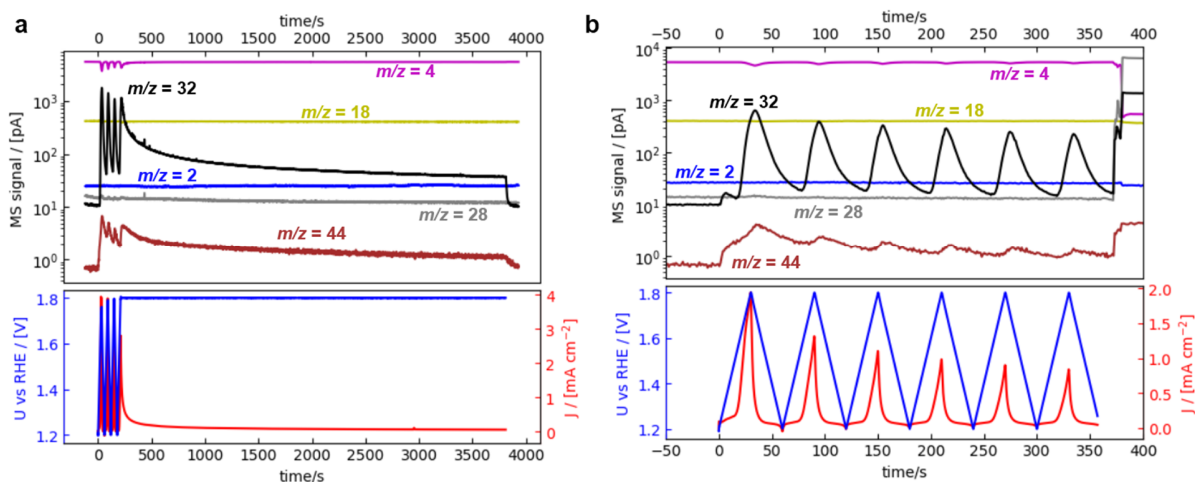
Supplementary Figure 19. a, The EC-MS raw data of Au-supported mass-selected IrO_2 catalyst in 0.1 M
$HClO_4$. **b,** The continuous experiment after experiment **(a)**. The upper panel shows the MS signals for H_2
($m/z = 2$, blue), He ($m/z = 4$, violet), H_2O ($m/z = 18$, yellow), N_2 or ^{12}CO ($m/z = 28$, gray), O_2 ($m/z = 32$,
black), and CO_2 ($m/z = 44$, red). The lower panel shows the potential (blue, left axis) and current density
(red, right axis) vs. time (s). We attribute the deactivation that occurs without such a low cathodic potential
to the oxidation of the gold substrate, because the same deactivation and reactivation phenomenon was also
observed on Au supported mass-selected IrO_2. The Au-supported IrO_2 was tested between 1.2 to 1.8 V vs.
RHE and then held the potential at 1.8 V vs. RHE for 1 h. As shown in Supplementary Figure 19a, the MS
O_2 signal decreases from the starting *ca.* 10^3 to *ca.* 10 pA. After that, experiment **(a)** was stopped, and the
working electrode was rested at OCP. It can be seen that in Supplementary Figure 19b, the MS O_2 signal
of the 1st cycle is recovered back to ~10^3 pA level after resting under OCP.
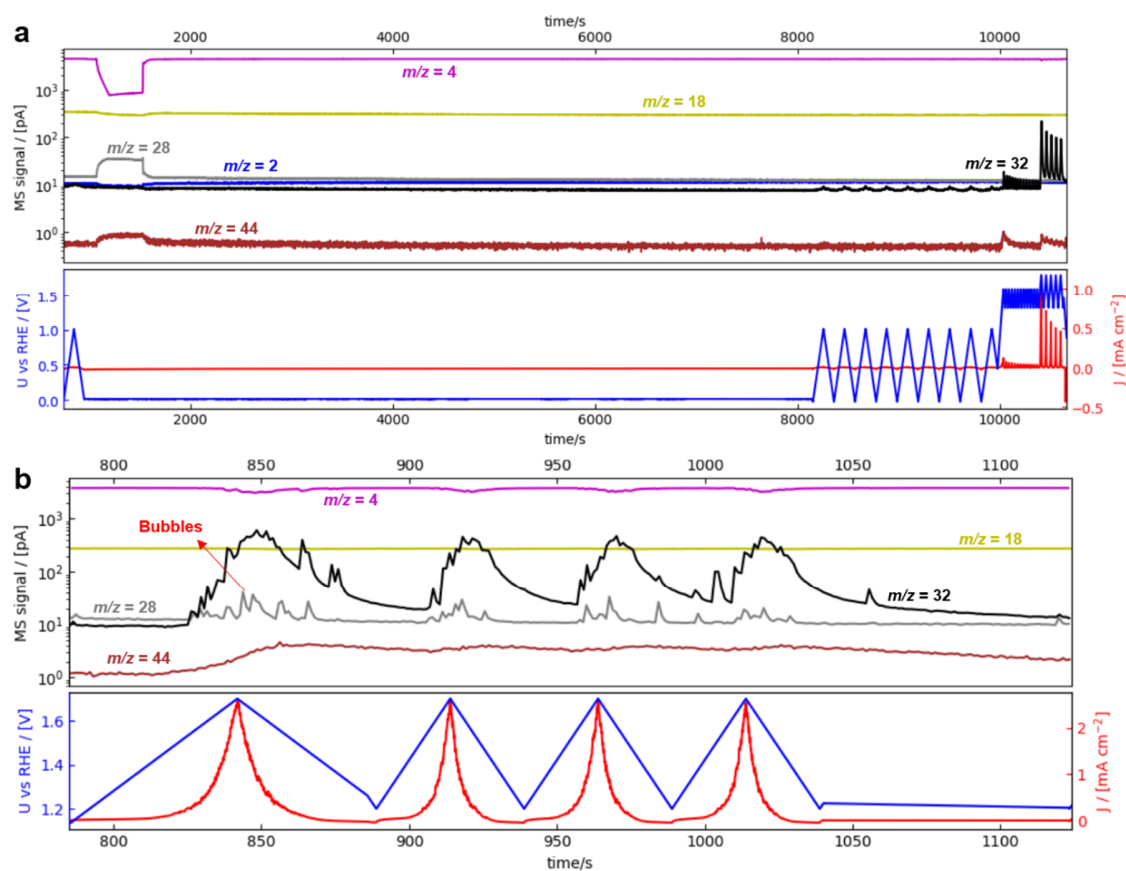
Supplementary Figure 20. Excluding the bubble formation induced deactivation during EC-MS measurements. a, The EC-MS raw data of mass-selected $Ir_{0.1}Ta_{0.9}O_{2.45}$ catalyst in 0.1 M $HClO_4$. **b,** One failed EC-MS experiment, due to the bubble formation. The upper panel shows the MS signals for H_2 (*m/z* = 2, blue), He (*m/z* = 4, violet), H_2O (*m/z* = 18, yellow), N_2 or ^{12}CO (*m/z* = 28, gray), O_2 (*m/z* = 32, black), and CO_2 (*m/z* = 44, red). The lower panel shows the potential (blue, left axis) and current density (red, right axis) vs. time (s). As shown in Supplementary Figure 20a, the background signals of N_2 (*m/z* = 28) and O_2 (*m/z* = 32) are stable. Once there are any bubbles formed (Supplementary Figure 20b), the MS N_2 (*m/z* = 28) and O_2 (*m/z* = 32) signals will emerge with unexpected sharp peaks. Therefore, based on the MS N_2 and O_2 background signals, we could easily observe the bubble formation.
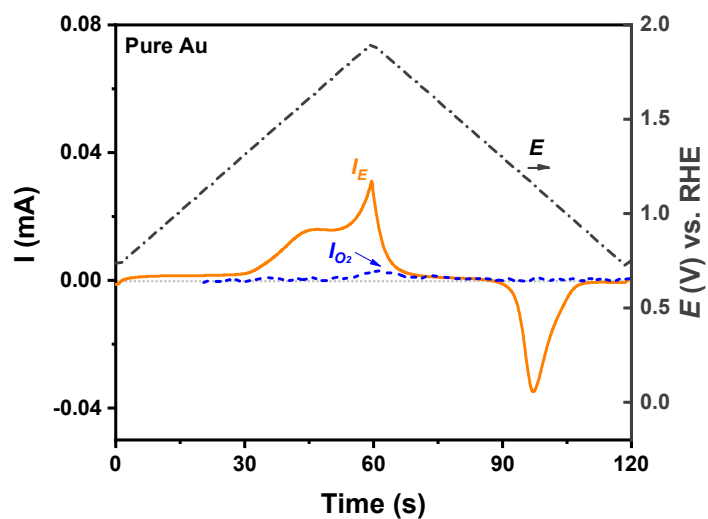
Supplementary Figure 21. Comparison of the electrochemical current (I_E) and the O$_2$ current (I_{O_2}, back-calculated from MS signal of $m/z = 32$) on pure Au electrode during potential cycling between open-circuit potential and 1.9 V vs. RHE with a scan rate of 20 mV s^{-1} in 0.1 M HClO$_4$. A tiny MS O$_2$ signal was detected when the potential reach close to 1.9 V vs. RHE, suggesting that Au is OER inactive at a lower potential range. The redox couple at *ca.* 45 and 100 s are due to the Au oxidation and reduction, respectively.
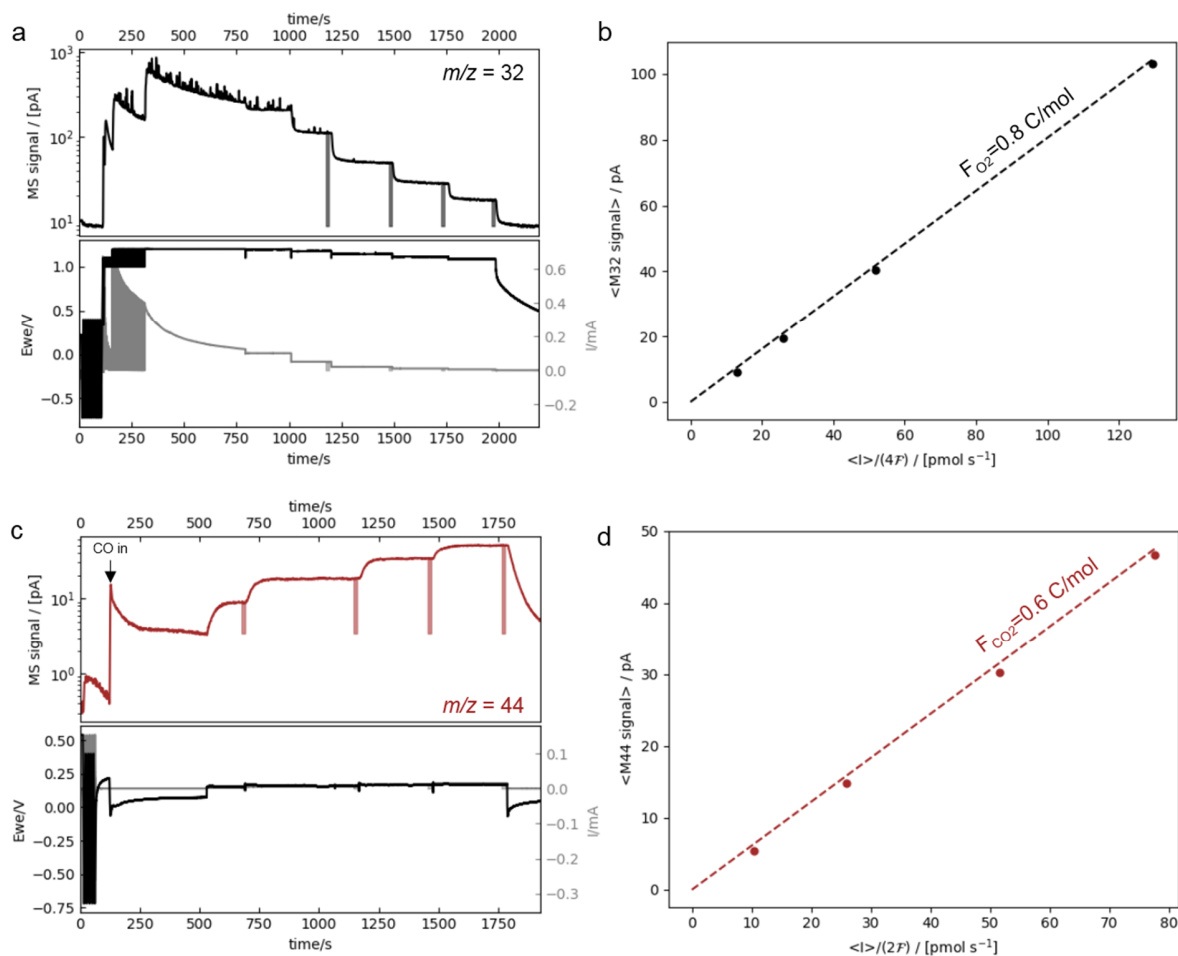
Supplementary Figure 22. O_2 and CO_2 calibrations of EC-MS. a-b, Calibration for O_2 by OER on Pt working electrode in 0.1 M $HClO_4$. Before the O_2 calibration, the Pt electrode was held at 2.0 V vs. RHE for 8 min. This ensures a 100% OER faradaic efficiency and avoids any charge lost to electrode surface oxidation. **c-d**, Calibration for CO_2 by CO oxidation using Pt working electrode in 0.1 M $HClO_4$. Bottom panel: Electrochemical potential and current. Top panel: mass spectrometer signal for $m/z = 32$ (O_2) and $m/z = 44$ (CO_2). The resulting calibration curves are plotted for O_2 and CO_2 as near-steady-state signal vs production rate, which are the respective sensitivity factors.
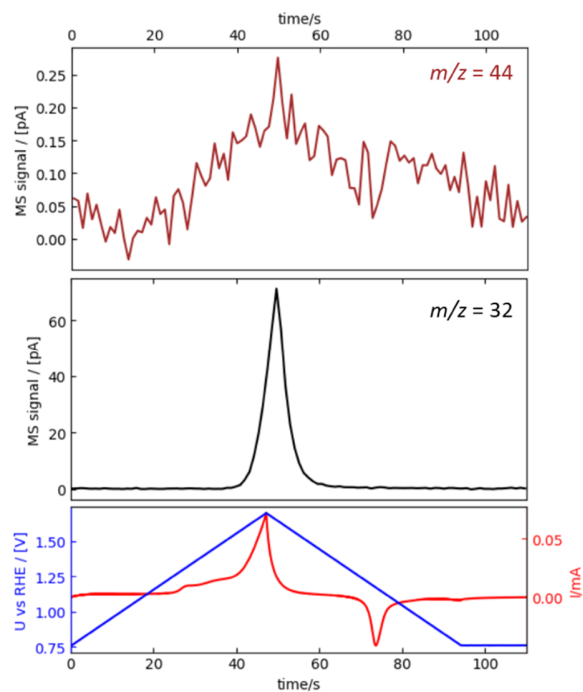
Supplementary Figure 23. Adventitious carbon decomposition during OER of gold supported 1.2×10^4 amu $Ir_{0.1}Ta_{0.9}O_{2.45}$ NPs with a scan rate of 20 mV s^{-1} in 0.1 M HClO$_4$. Carbon can be oxidized partially during OER, not releasing CO$_2$, therefore, the FE of carbon oxidation in the main text is a lower bound.
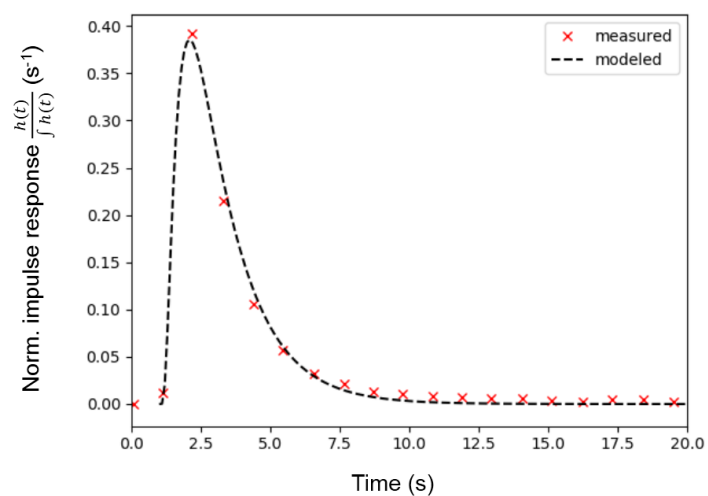
Supplementary Figure 24. EC-MS impulse response test for determining the distance between the electrode surface and Si chip. The predicted and measured area-normalized impulse responses match well is important to ensure accurate deconvolution. More explanations could be found in our recent publication[10].
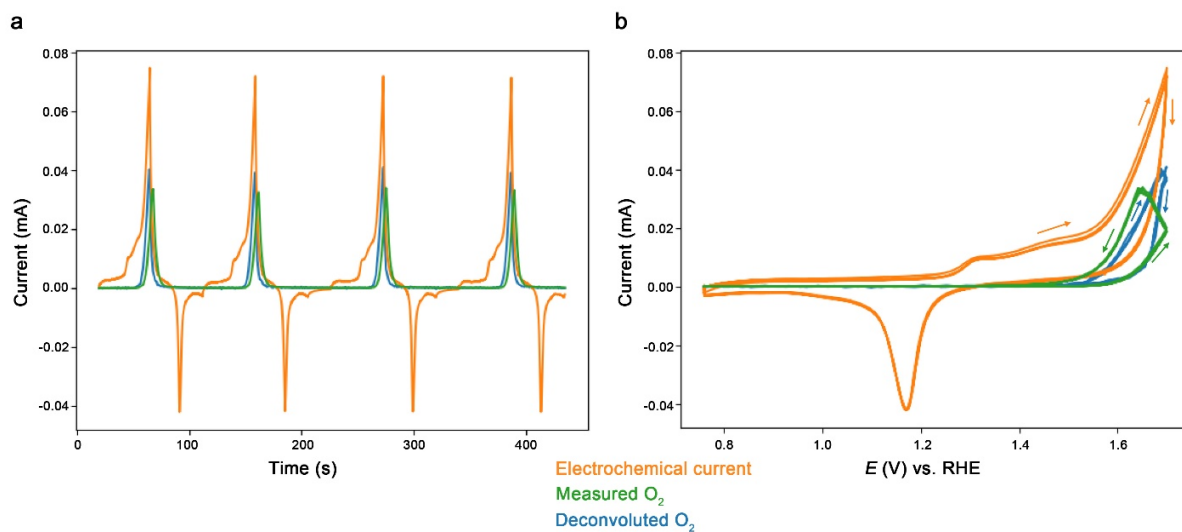
Supplementary Figure 25. Comparison of electrochemical current, measured O_2 current, and deconvoluted O_2 current of gold supported 1.2×10^4 amu $Ir_{0.1}Ta_{0.9}O_{2.45}$ catalyst. The arrows in (b) represent the cyclic sweeping direction.
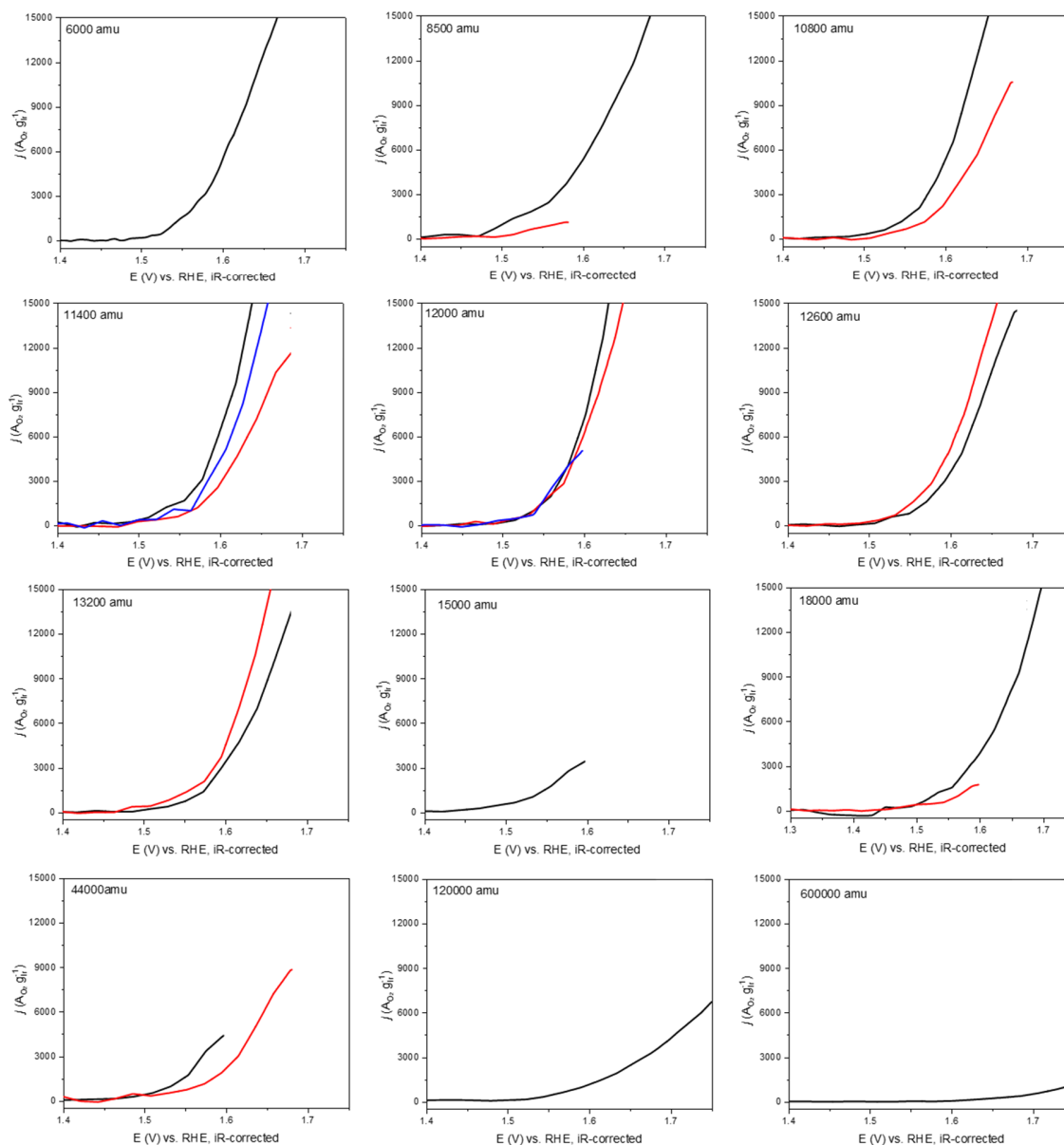
Supplementary Figure 26. The OER activity overview of the studied mass-selected $Ir_{0.1}Ta_{0.9}O_{2.45}$ NPs. Scan rate: 20 mV s^{-1}, 0.1 M HClO$_4$. The OER activity of our studied samples were assessed by using forward anodic-going sweep of the deconvoluted O$_2$ current. Three (1.14×10^4 and 1.2×10^4 amu) or two (8.50×10^3, 1.08×10^3, 1.26×10^4, 1.32×10^4, 1.80×10^4, and 4.4×10^4 amu) independent $Ir_{0.1}Ta_{0.9}O_{2.45}$ samples were measured. We have studied 12 different sizes of mass-selected $Ir_{0.1}Ta_{0.9}O_{2.45}$ NPs, the sizes of 1.14×10^4 and 1.2×10^4 amu particles have been tested three times to check the uncertainties. Since, the preparation and the electrochemical measurements were conducted with the exact same protocols, the uncertainty should be representative for all the other sizes.
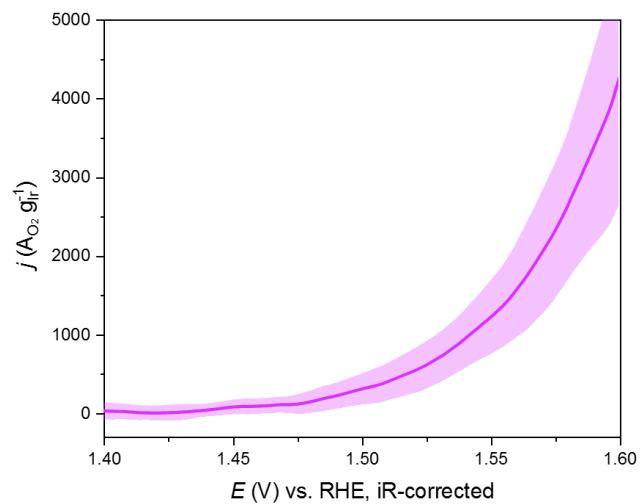
Supplementary Figure 27. The average mass activity and standard deviation of 20 independent mass-selected $Ir_{0.1}Ta_{0.9}O_{2.45}$ catalysts in a small size regime of 1-2 nm. Scan rate: 20 mV s^{-1}, 0.1 M $HClO_4$.
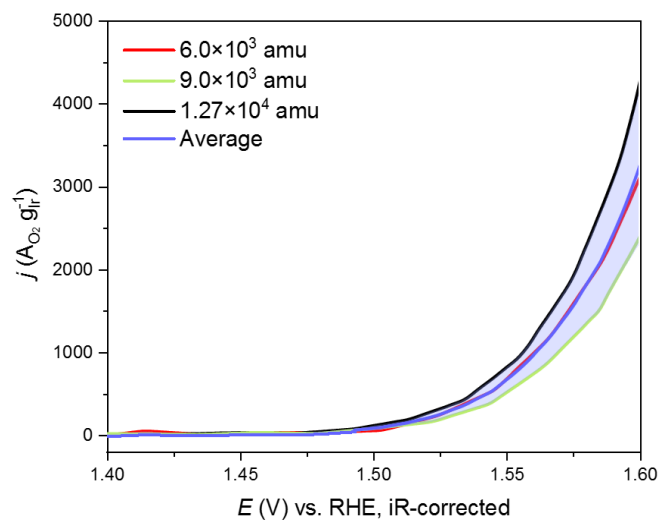
Supplementary Figure 28. EC-MS determined OER activities of mass-selected IrO$_2$ NPs. Scan rate: 20 mV s^{-1}, 0.1 M HClO$_4$. Average and standard deviation are based on three independent mass-selected IrO$_2$ catalysts (6.0×10^3, 9.0×10^3, and 1.27×10^4 amu particles).
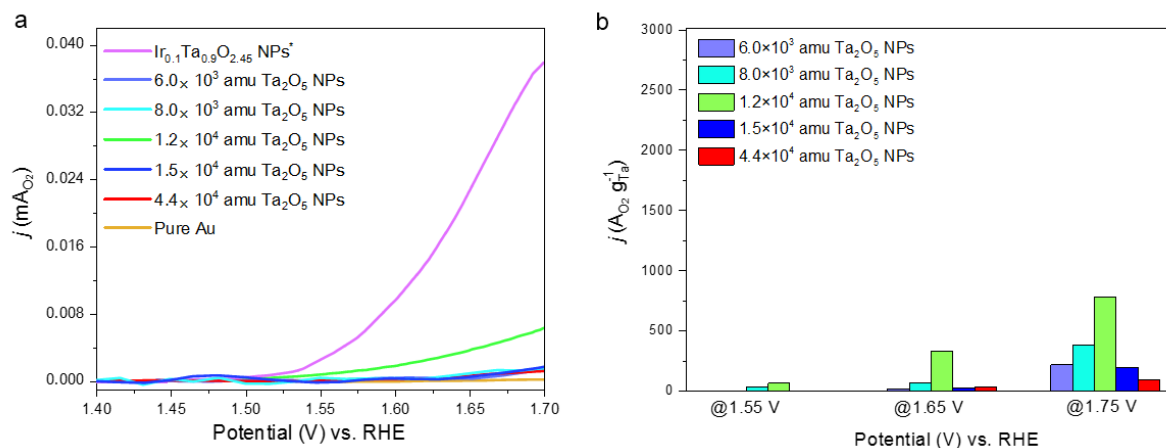
Supplementary Figure 29. a, Comparison of the EC-MS determined OER current between $Ir_{0.1}Ta_{0.9}O_{2.45}$ NP*, different mass-selected Ta_2O_5 catalysts, and pure gold electrode. $Ir_{0.1}Ta_{0.9}O_{2.45}$ NP* represents the average activity of all mass-selected $Ir_{0.1}Ta_{0.9}O_{2.45}$ catalysts, which are smaller than 2 nm. Scan rate: 20 mV s^{-1}, 0.1 M $HClO_4$. **b,** The mass activities (normalized to the total Ta loading) of mass-selected Ta_2O_5 NPs at different overpotentials. Pure mass-selected Ta_2O_5 NPs only perform OER activity at high working potential.
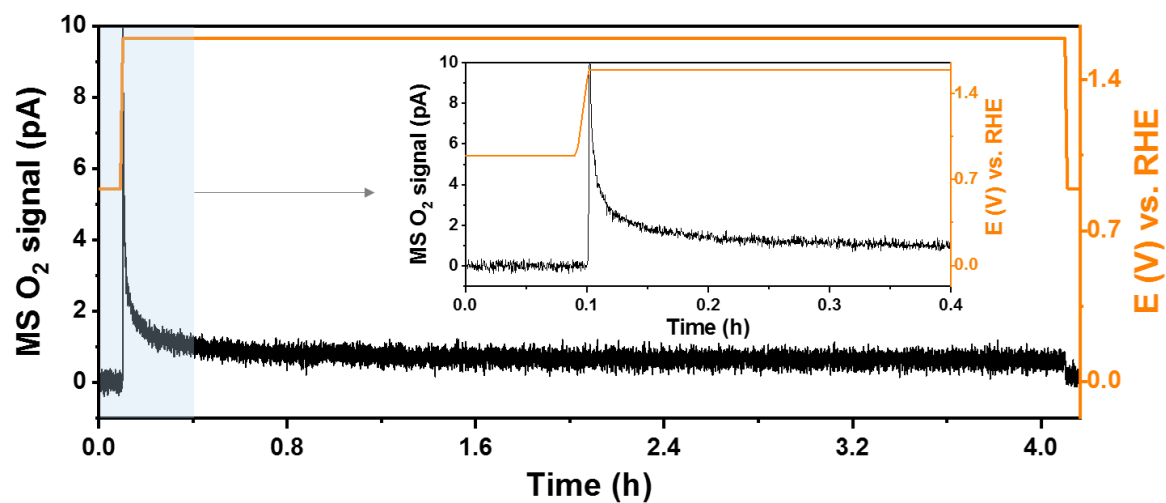
Supplementary Figure 30. Stability performance of the 4.4×10^4 amu $Ir_{0.1}Ta_{0.9}O_{2.45}$ catalyst at 1.6 V vs. RHE for the first 4 h experiment in 0.1 M $HClO_4$. The inset is the amplification of the first 0.4 h curve. Before measurment, the electrode was holding a potential at OCP (*ca.* 0.8 V vs. RHE), after that the potential was stepped up to 1.6 V vs. RHE, and the MS O_2 signal dropped suddenly within minutes. The OER activity of our catatlyst could be recovered after reducing the Au electrode at OCP (as shown in main text), suggesting the robust stability of mass-selected $Ir_{0.1}Ta_{0.9}O_{2.45}$ catalyst.
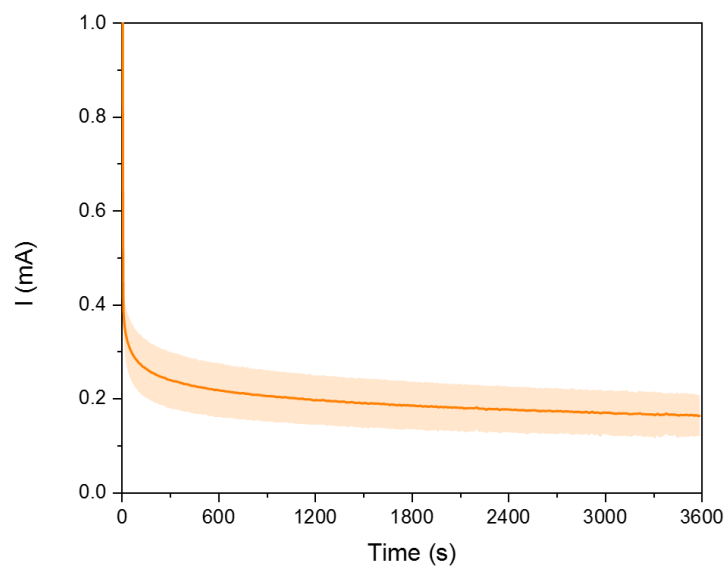
Supplementary Figure 31. Chronoaperonmetric measurements of sputtered $IrTa_9O_x$ thin film samples in 0.1 M $HClO_4$ at 570 mV overpotential and 1600 rpm on a rotating disk electrode setup. The average current and the standard deviation are from three independent $IrTa_9O_x$ thin film samples. The $IrTa_9O_x$ thin film samples were deposited on Au electrode at 400 °C by reactive sputtering the $IrTa_9$ target in the O_2+Ar atmosphere at a total pressure of 3 mTorr. After 1h, the electrolyte was collected for further ICP-MS analysis. The S-number of $IrTa_9O_x$ thin film was calculated based on the amount of evolved oxygen (calculated from Q_{total}) and the dissolved Ir (obtained from ICP-MS).
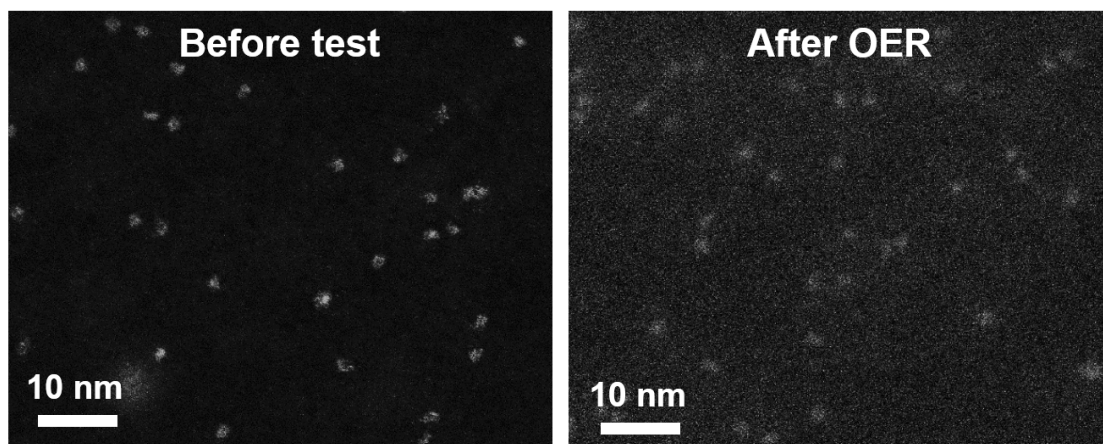
Supplementary Figure 32. ADF-STEM images of mass-selected 1.2×10^4 amu $Ir_{0.1}Ta_{0.9}O_{2.45}$ NPs before and after electrochemical test. To investigate the morphology stability of our catalyst, 2 % coverage of mass-selected 1.2×10^4 amu $Ir_{0.1}Ta_{0.9}O_{2.45}$ NPs were deposited on gold TEM grids. The ADF-STEM images were collected before and after two CV cycles at 20 mV s^{-1} up to 1.6 V vs. RHE in 0.1 M $HClO_4$. Each experiment was repeated more than 20 times with similar results.
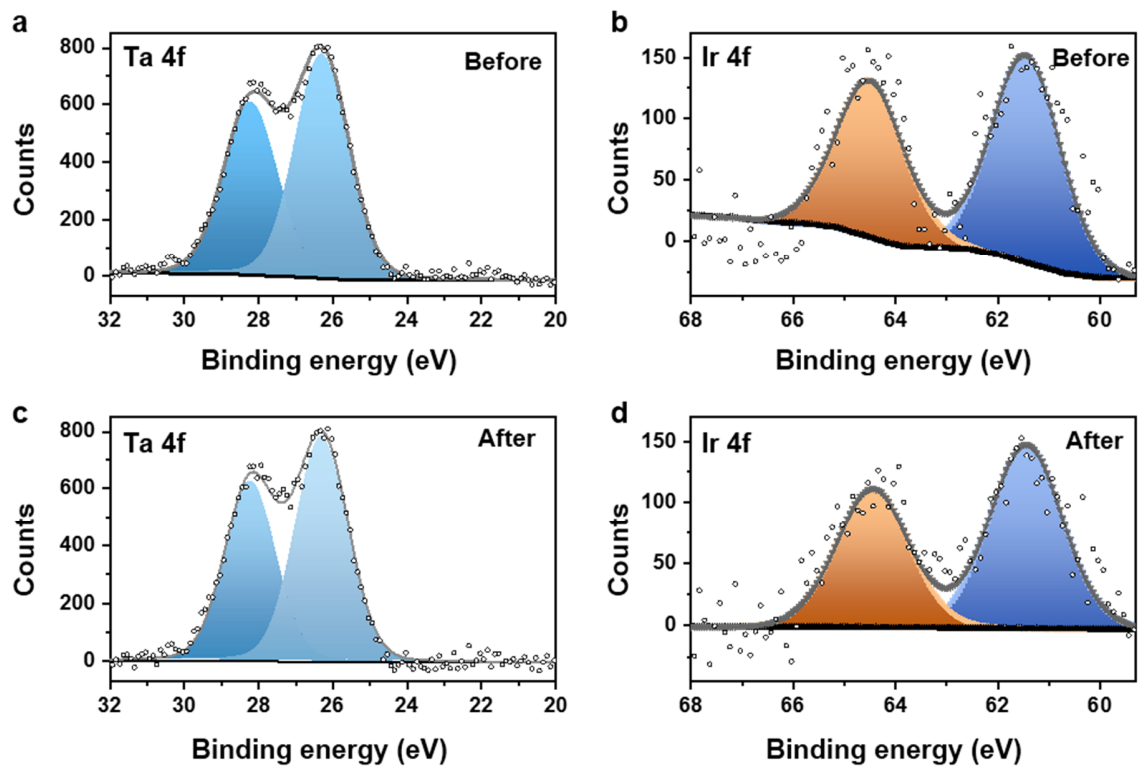
Supplementary Figure 33. Ta 4f and Ir 4f spectra of mass-selected 1.2×10^5 amu $Ir_{0.1}Ta_{0.9}O_{2.45}$ NPs before (a-b) and after (c-d) electrochemical tests.

a CO

Ir

Ta

O

ΔG_{CO} = -1.49 eV

Ir-doped Ta$_2$O$_5$ (200)

b CO

ΔG_{CO} = 0.13 eV
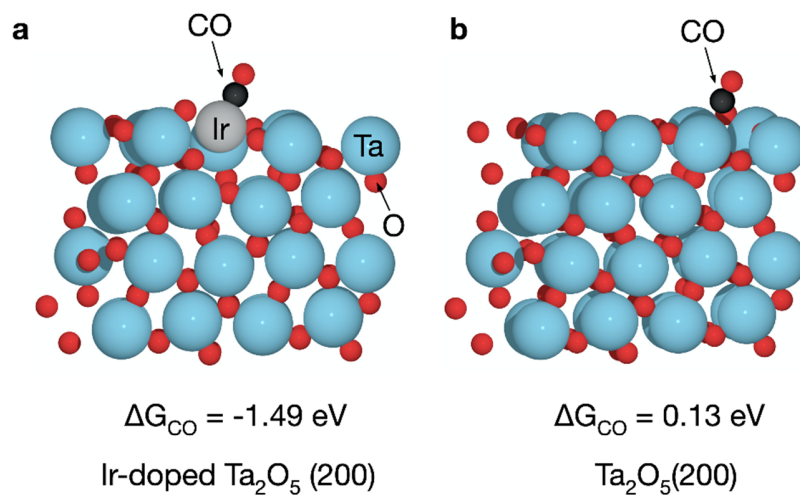
Ta$_2$O$_5$(200)

Supplementary Figure 34. Calculated CO adsorption free energy (ΔG_{CO}) on Ir-doped Ta$_2$O$_5$ (200) and Ta$_2$O$_5$ (200) surfaces.
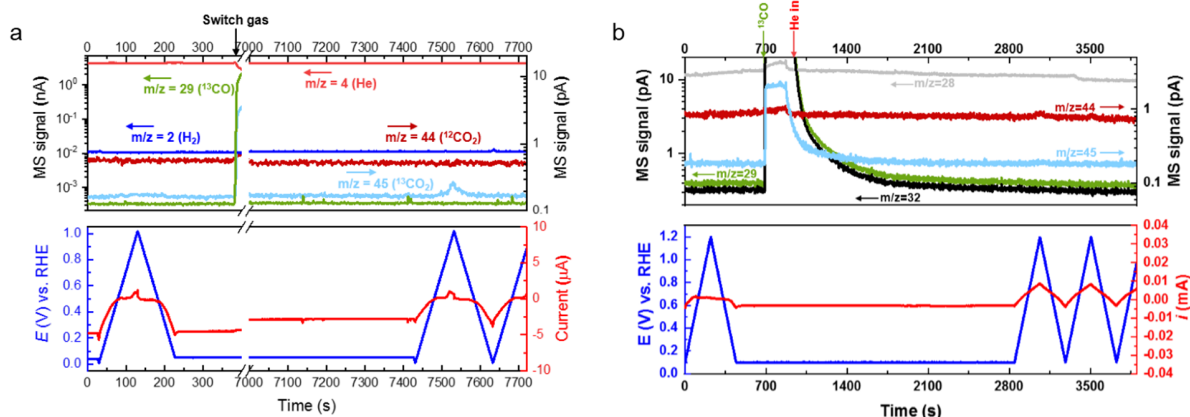
Supplementary Figure 35. ^{13}C isotope-labeling combined EC-MS to determine surface Ir active sites. **a,** Measurement of mass-selected 1.8×10^4 amu $Ir_{0.1}Ta_{0.9}O_{2.45}$ catalyst by EC-MS in 0.1 M $HClO_4$. **b,** ^{13}CO stripping on gold supported mass-selected 1.2×10^4 amu Ta_2O_5 NPs. The upper panel shows the MS signals for H_2 ($m/z = 2$, blue), He ($m/z = 4$, coral), N_2 or ^{12}CO ($m/z = 28$, gray), and ^{13}CO ($m/z = 29$, green) on the left axis, and the signals for $^{12}CO_2$ ($m/z = 44$, red) and $^{13}CO_2$ ($m/z = 45$, cyan) on the right axis. The lower panel shows the potential (blue, left axis) and current density (red, right axis) vs. time (s). Significant CO oxidation does not occur on IrO_2 surface until after the cathodic sweep to potentials lower than 0.1 V vs. RHE, which indicates that CO stripping can only be conducted on the reduced IrO_2 surface[11]. In our study, when introducing ^{13}CO gas to the electrolyte, the working electrode was held at 0 V vs. RHE, and the surface Ir site of $Ir_{0.1}Ta_{0.9}O_{2.45}$ catalyst could be reduced to bind CO. Iridium behaves very similar to platinum in its interaction with carbon, which can be seen by comparing base cyclic voltammetry and CO oxidation on Ir film with those on Pt electrode. Due to the low Ir loading of mass-selected $Ir_{0.1}Ta_{0.9}O_{2.45}$ particles, the coverage effect on Ir has not been considered, therefore, we assume each Ir site adsorb one CO molecule.
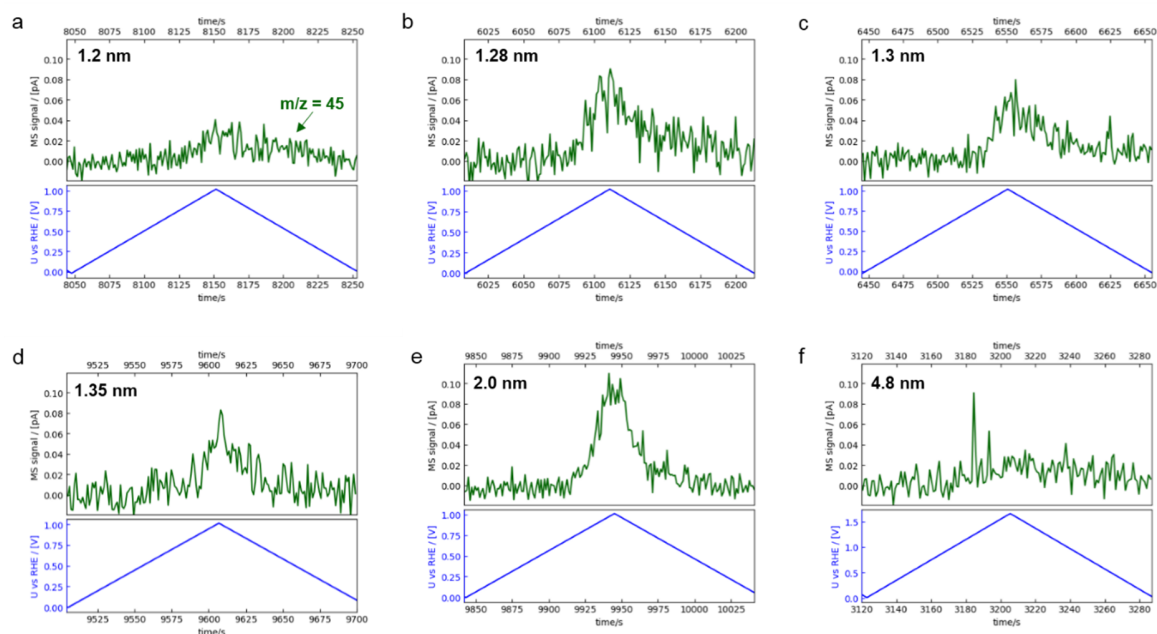
Supplementary Figure 36. MS signals of $^{13}CO_2$ (*m/z* = 45, green) after ^{13}CO stripping on different gold supported mass-selected $Ir_{0.1}Ta_{0.9}O_{2.45}$ NPs. The number of sites was calculated by integrating the calibrated $^{13}CO_2$ signal over the 200 seconds of the measurement, as shown in Supplementary Figure 33. Calibration was performed by bulk CO oxidation on a platinum electrode as described in reference[12]. The background on these signals was subtracted such that the integrated signal over the first 30 seconds of the data shown is zero. In other words, the baseline m/z = 45 MS signal is defined just before the onset of the striping signal. To avoid the overlap of the particles, the deposition of mass-selected nanoparticles on the electrode is controlled to be 5% projected surface area coverage, and the catalyst loading was calculated according to the deposition current and deposition time, as described in Methods. The loading increased with the increase of particle size, as concluded in Supplementary Table 1. Therefore, the $^{13}CO_2$ MS signal of the larger nanoparticles (high Ir loading) is higher than the signal of the smaller nanoparticles (low Ir loading). Due to the high atomic exposure structure of small size $Ir_{0.1}Ta_{0.9}O_{2.45}$ NPs (< 2 nm), they show a similar surface Ir ratio of 20~40 %. As the particle size increases further, such as 4.8 nm NPs, the particle tend to be spherical, most Ir atoms are trapped inside the particles during the oxidation process, and fewer Ir atoms are exposed on the surface. So after CO stripping on the 4.8 nm sample, the $^{13}CO_2$ MS signal is lower than other sizes.

Supplementary Table 1. Preparation of mass-selected Ir-Ta, Ir, and Ta particles with 5% coverage on the polycrystalline Au support.

Mass-selected particle	Calculated diameter (nm)	Number of atoms in each particle	Number of deposited particles	Total mass loading (ng cm^{-2})	Ir loading (ng cm^{-2})
6,000 AMU IrTa$_9$	1.0	33	1.17×10^{12}	59.5	6.3
8,500 AMU IrTa$_9$	1.2	47	9.28×10^{11}	67.0	7.1
10,800 AMU IrTa$_9$	1.25	59	7.91×10^{11}	72.4	7.7
11,400 AMU IrTa$_9$	1.28	63	7.63×10^{11}	73.7	7.8
12,000 AMU IrTa$_9$	1.3	66	7.35×10^{11}	74.7	7.9
12,600 AMU IrTa$_9$	1.32	73	7.14×10^{11}	76.2	8.0
13,200 AMU IrTa$_9$	1.35	73	6.92×10^{11}	77.6	8.2
15,000 AMU IrTa$_9$	1.4	83	6.35×10^{11}	80.6	8.5
18,000 AMU IrTa$_9$	1.5	99	5.63×10^{11}	85.7	9.0
44,000 AMU IrTa$_9$	2.0	242	3.10×10^{11}	115.3	12.2
120,000 AMU IrTa$_9$	2.8	659	1.59×10^{11}	161.1	17.0
600,000 AMU IrTa$_9$	4.8	3295	5.43×10^{10}	274.5	29.0
6,000 AMU Ir	1.0	31	1.40×10^{12}	71.2	71.2
9,000 AMU Ir	1.1	47	1.07×10^{12}	81.6	81.6
12,700 AMU Ir	1.3	66	8.48×10^{11}	91.2	91.2
6,000 AMU Ta	1.0	33	1.14×10^{12}	58.2	N/A
8,000 AMU Ta	1.1	44	9.44×10^{11}	63.8	N/A
12,000 AMU Ta	1.3	66	7.19×10^{11}	73.2	N/A
15,000 AMU Ta	1.4	83	6.21×10^{11}	79.1	N/A
44,000 AMU Ta	2.0	243	2.30×10^{11}	85.7	N/A

Supplementary Table 2. Calculated surface energies (γ) of λ-Ta$_2$O$_5$ with maximum surface miller indexes of two.

Low index facets	γ(J/m^2)	high index facets	γ(J/m^2)
(110)	0.26, 0.28	(210)	0.30, 0.32
(100) (equiv. (200))	0.30	(120)	0.39
(010)	0.35	(021)	0.59
(111)	0.63	(102)	0.74
(011)	1.02	(121)	0.94
(101)	1.04	(201)	1.08
(001)	1.74		

The surface energy (γ) was calculated by $\gamma = (E_{slab} - nE_{bulk})/2A$, where E_{slab} and E_{bulk} are electronic total energies of the surface and bulk unit cell, respectively. n is the number of bulk unit cell in the slab. A is the surface area of the slab. Supplementary Table 2 summarizes the calculated surface energies for λ-Ta$_2$O$_5$. The five facets, (110), (210), (200), (120), (010) with the lowest surface energy were selected to investigate the OER activity. The stability of the doped Ir was first evaluated by comparing the electronic energies of Ir located at the topmost layer and subsurface layer. It is found Ir is only stable in the (200) topmost layer and all other facets tend to have Ir located in the subsurface. The (200) surface was finally chosen for the activity calculations.
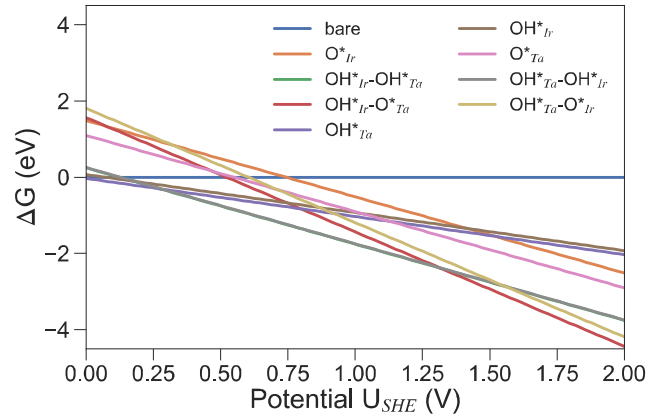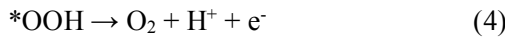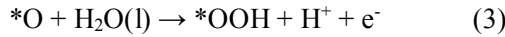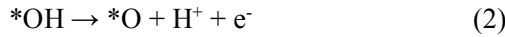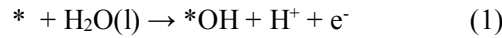
Supplementary Figure 37. Calculated surface Pourbaix diagrams of Ir-doped $Ta_2O_5(200)$ with all possible coverage configurations at pH = 0. The surface Pourbaix diagram was constructed to identify the most stable adsorbates at the surface of a catalyst under OER working conditions. It can be seen that at the potential of 1.23 - 1.70 V, the surface of Ir-doped $Ta_2O_5(200)$ is predicted to be covered by OH* and O* at the Ir and Ta sites, respectively.

Supplementary Note 1：Surface pourbaix diagram of Ir-doped $Ta_2O_5(200)$

The OER activity was evaluated by calculating the theoretical overpotential of the elementary steps in the reaction mechanism proposed in prior works[13-15], which is given by:

$$* + H_2O(l) \rightarrow *OH + H^+ + e^- \qquad (1)$$

$$*OH \rightarrow *O + H^+ + e^- \qquad (2)$$

$$*O + H_2O(l) \rightarrow *OOH + H^+ + e^- \qquad (3)$$

$$*OOH \rightarrow O_2 + H^+ + e^- \qquad (4)$$

where * represents a surface site. The reaction energy of these elementary steps was calculated as:

$$\Delta G_1 = \Delta G_{OH}$$

$$\Delta G_2 = \Delta G_O - \Delta G_{OH}$$

$$\Delta G_3 = \Delta G_{OOH} - \Delta G_O$$

$$\Delta G_4 = 4.92 - \Delta G_{OOH}$$

The adsorption free energy of each adsorbate (*O, *OH, *OOH) was calculated at 0 V vs RHE by referencing to the liquid water and hydrogen gas at standard conditions and as given by $\Delta G_{ads} = \Delta E_{ads} + \Delta G_{correction}$ where ΔE_{ads} is the DFT calculated binding energy of each adsorbate. $\Delta G_{correction}$ is free energy correction of adsorbates, including zero-point energy, integrated heat capacity from 0 K to 298.15 K and entropy. Based on the harmonic approximation, the calculated $\Delta G_{correction}$ for *O, *OH, *OOH are 0.06 eV, 0.31 eV, 0.40 eV, respectively. The theoretical overpotential was therefore determined by $min(\Delta G_1, \Delta G_2, \Delta G_3, \Delta G_4)$. The OER volcano of theoretical overpotentials was then plotted with respect to the OER activity descriptor, $\Delta G_O - \Delta G_{OH}$. In this method the charge and solvation effects are neglected, though some works show that they are useful in interpreting certain experimental phenomena in electrocatalysis[16-18].
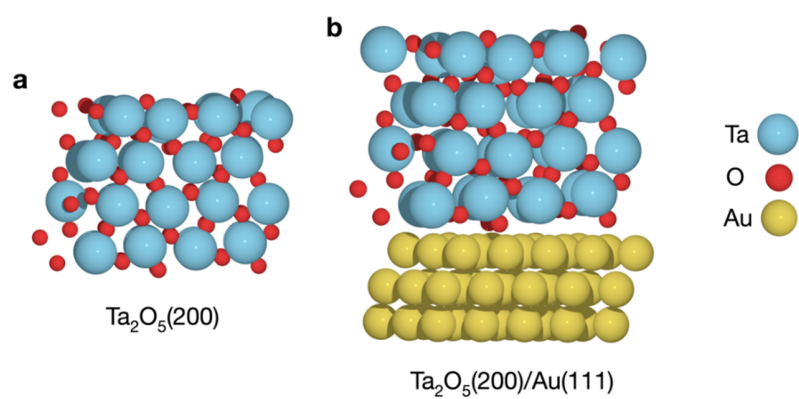
Supplementary Figure 38. Structure representations of Ta_2O_5 (200) and Au supported Ta_2O_5 (200) surfaces.
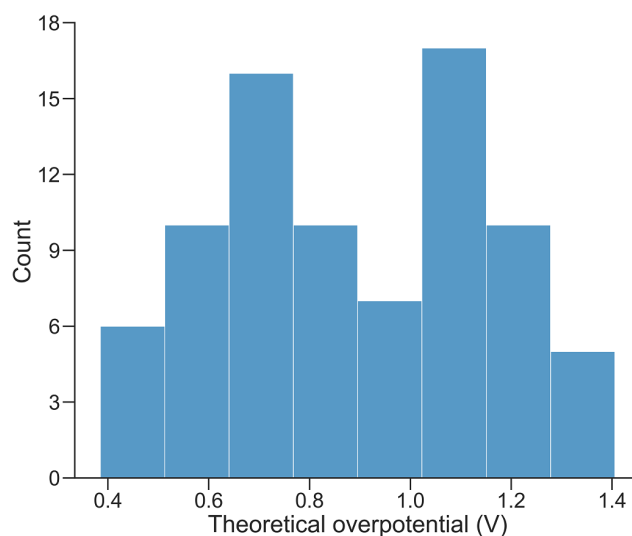
Supplementary Figure 39. Distribution of calculated theoretical overpotentials for 50 lowest energy structures of 30 metal-atoms oxide cluster model. The raw data are provided in the supplementary worksheet.

Supplementary Note 2：OER activity calculations using Ir-Ta-O cluster models

Methods. The structure determination of an oxide cluster with large number of atoms (e.g. number of atoms > 100) based on density functional theory (DFT) calculations is still a great challenge because of the high computational cost. To identify energetically favorable structures of $Ir_{0.1}Ta_{0.9}O_{2.45}$ cluster, we first determined the structure of Ta_2O_5 clusters and then doped Ir into the identified lowest energy configuration. Because it is too computationally expensive to search the energetically favorable structures of ternary clusters using global structure optimization. This determination is expected to be reasonable at low Ir doping concentration. Structures of Ta_2O_5 clusters were determined using a machine-learning aided global structure optimization, which has been shown to be two orders of magnitude faster than the conventional global optimization algorithm[19]. In this global structure search, we took advantage of the linear combination of atomic orbitals method implemented in GPAW to calculate the total energy with the PBE functional[20]. A double zeta polarized (dzp) basis and a grid spacing of at least 0.2 Å were used. Structures were optimized using the BFGSLineSearch algorithm as implemented in ASE with a force convergence criterion of 0.05 eV/ Å (ref. [21]). Using the above approach, we performed global structure search for two Ta_2O_5 cluster with compositions of $Ta_{30}O_{75}$ and $Ta_{66}O_{165}$. Three and six Ir atoms were randomly doped into the identified structures of $Ta_{30}O_{75}$ (denoted as *30 metal-atoms cluster*) and $Ta_{66}O_{165}$ (denoted as *66 metal-atoms cluster*), respectively, to mimic the experimental Ir:Ta ratio of 1:9. The OER activity of clusters were calculated using the all-electron code FHI-aims with the RPBE functional[22]. The light basis set was used, and convergence tests show that the difference in calculated theoretical overpotentials between using light and tight basis set is small (< 0.06 V). Scalar relativistic effects were included via the zeroth-order relativistic approximation (ZORA) (ref. [23]).

Results. To simulate the studied mass-selected $Ir_{0.1}Ta_{0.9}O_{2.45}$ NP structure, we also investigated the OER activity for some cluster structures determined using a machine learning-aided global structure optimization strategy[19]. Given the fact that there is some uncertainty in the predicted clusters structures, we performed OER activity calculations for 50 lowest energy structures based on the 30 metal-atoms cluster model. The largest difference in the calculated formation enthalpies of these 50 lowest energy structures is 11 meV/atom. This small difference in relative phase stabilities suggests that all these structures are likely to

be accessible in thermodynamics. The calculated theoretical overpotentials for these 50 structures are plotted in Supplementary Figure 39. There are six structures having calculated theoretical overpotentials lower than $IrO_2(110)$ (0.49 V) and the smallest calculated overpotential is 0.39 V. It is generally believed that the active site would mostly dominate the catalytic reaction regardless of its appearance. It is therefore concluded that similar to Ir-doped $Ta_2O_5(200)$ surface, Ir-doped Ta_2O_5 clusters may have an excellent OER activity.

Structure representation of the 30 metal-atoms oxide cluster that has the lowest calculated theoretical overpotential:
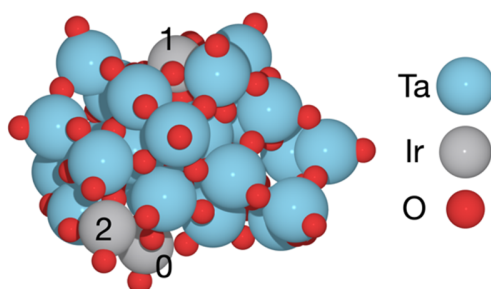
Supplementary Table 3. The calculated theoretical overpotentials for Ir sites on 30 metal-atoms oxide cluster structure that has the lowest calculated theoretical overpotential. There are three Ir atoms in this structure. Two of them were calculated for OER activity and the last one is unavailable for activity evaluation because it binds O* too strong.

Ir site index	ΔG_O-ΔG_{OH} (eV)	Theoretical overpotential (V)
0	0.70	1.21
1	1.36	0.39

Due to the high computational cost of doing DFT-calculations for 66 metal-atoms oxide clusters (~ 230 atoms), we only performed the OER activity calculation for the most stable cluster structure. Supplementary Table 3 shows the calculated theoretical overpotentials for all Ir sites in this structure. The most active Ir site has a calculated theoretical overpotential of 0.36 V, which is close to that (0.39 V) of 30 metal-atoms cluster and lower than that (0.49 V) of $IrO_2(110)$.

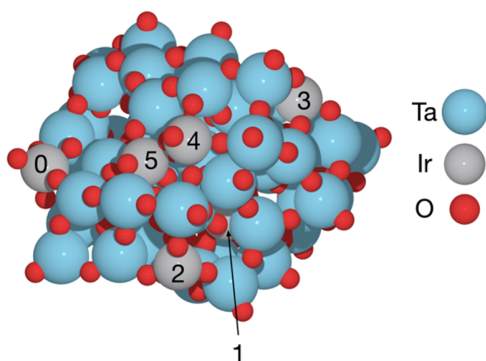Illustration of the calculated most stable structure of 66 metal-atom oxide cluster is shown below:

Supplementary Table 4. The calculated theoretical overpotentials for Ir sites on 66 metal-atoms oxide cluster. There are six Ir atoms in this model. Three of them were calculated for OER activity and the rest are invalid for activity evaluation because of inaccessible Ir sites. (The Ir site with index 1 locates inside the cluster; The Ir site with index 3 is unstable when adsorbed with O^*/OH^*/OOH^*; The Ir site with index 5 locates in the subsurface.)

Ir site index	$\Delta G_O - \Delta G_{OH}$ (eV)	Theoretical overpotential (V)
0	1.47	0.53
2	1.59	0.36
4	0.69	1.13

To summarize, the calculated theoretical overpotentials of the most active Ir sites on 30-metal atoms ($Ir_3Ta_{27}O_{75}$) and 66 metal-atoms ($Ir_6Ta_{60}O_{165}$) are 0.39 V of 0.36 V, which are close to that (0.43 V) of Ir-doped Ta_2O_5 (200) surface, confirming that the Ir-doped Ta_2O_5 catalyst would have an excellent OER activity.
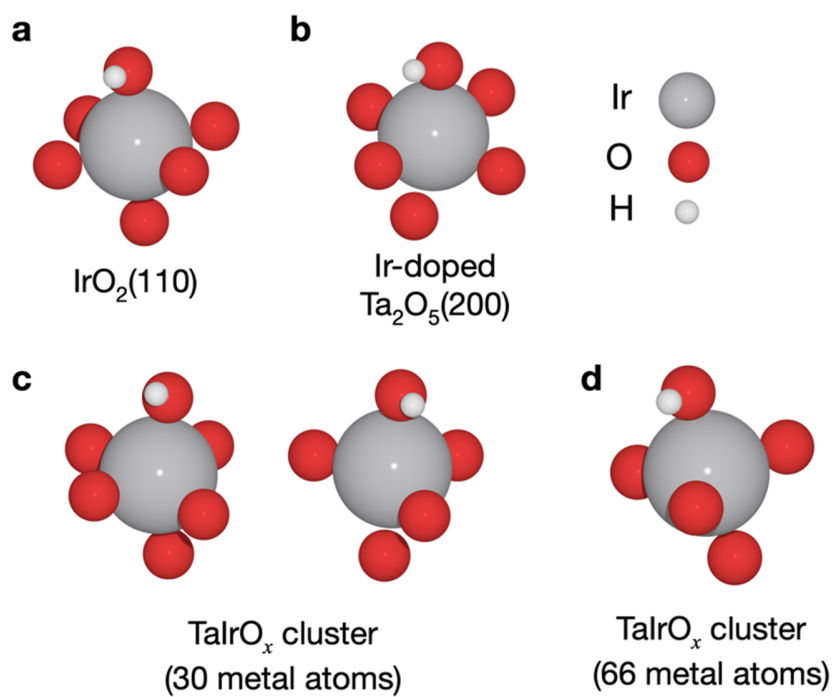
Supplementary Figure 40. Coordination of the active Ir sites for OER in (a) IrO_2(110) (b) Ir-doped Ta_2O_5 (200), (c) 30 metal-atoms and (d) 66 metal-atoms $Ir_{0.1}Ta_{0.9}O_{2.45}$ cluster. In the slab models, the Ir coordination is IrO_6, while in the cluster models, the Ir coordination could be IrO_6 or IrO_5.
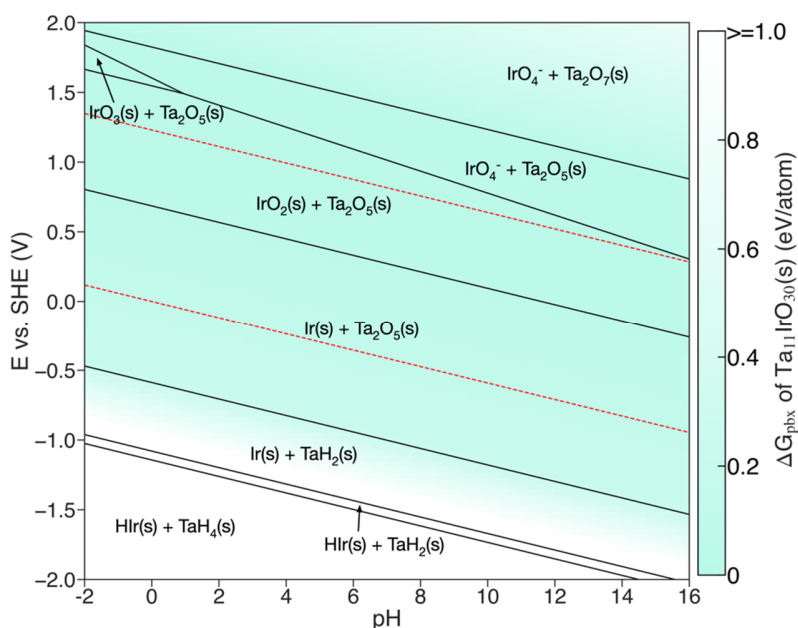
Supplementary Figure 41. Calculated Ir-Ta-O-H Pourbaix diagram with aqueous ions concentration 10^{-6} M at 25 °C. The Lake blue color gauges the aqueous stability of Ir-doped Ta_2O_5 ($Ta_{11}IrO_{30}$) at relevant potential and pH, which was represented by free energy difference (ΔG_{pbx}) between the studied compound and the most stable species at the given potential and pH.

Supplementary Note 3: DFT calculations of OER stability

The catalyst stability under OER operating conditions was evaluated using the DFT-calculated bulk Pourbaix diagram. All materials in the chemical space Ir-Ta-O-H from the Materials Project were calculated for the stability analysis[12]. Though the exact structure of $Ir_{0.1}Ta_{0.9}O_{2.45}$ cluster is unknown in experiment, the bulk phase of Ir-doped Ta_2O_5, $IrTa_{11}O_{30}$ was adopted in the stability analysis to estimate the catalyst stability under working conditions. The Ir doping concentration in $IrTa_{11}O_{30}$ was 8.33%, which is close to the experimental value. This figure shows the DFT-calculated Pourbaix diagram for $IrTa_{11}O_{30}$. It is not surprising that $IrTa_{11}O_{30}$ does not appear in the Pourbaix diagram because $IrTa_{11}O_{30}$ is relatively metastable compared to the most stable phases of IrO_2 and Ta_2O_5. Note that only the most thermodynamically stable chemical species are shown in the conventional (2-dimentional) Pourbaix diagram.

Supplementary References

1   Secher, N. M. Mass-Selected Model Systems in Catalysis. *Ph.D. thesis* (2020).
2   De Backer, A., Van den Bos, K., Van den Broek, W., Sijbers, J. & Van Aert, S. StatSTEM: an efficient approach for accurate and precise model-based quantification of atomic resolution electron microscopy images. *Ultramicroscopy* **171**, 104-116 (2016).
3   Van Aert, S. *et al.* Procedure to count atoms with trustworthy single-atom sensitivity. *Phys. Rev. B* **87**, 064107 (2013).
4   De Backer, A., Martinez, G. T., Rosenauer, A. & Van Aert, S. Atom counting in HAADF STEM using a statistical model-based approach: methodology, possibilities, and inherent limitations. *Ultramicroscopy* **134**, 23-33 (2013).
5   Chastain, J. & King Jr, R. C. Handbook of X-ray photoelectron spectroscopy. *Perkin-Elmer Corporation* **40**, 221 (1992).
6   Dupin, J.-C., Gonbeau, D., Vinatier, P. & Levasseur, A. Systematic XPS studies of metal oxides, hydroxides and peroxides. *Phys. Chem. Chem. Phys.* **2**, 1319-1324 (2000).
7   Porkovich, A. *et al.* In Situ Observation of Metal to Metal Oxide Progression: A Study of Charge Transfer Phenomenon at Ru-CuO Interfaces. *Acs Nano* **13**, 12425-12437 (2019).
8   Krukau, A. V., Vydrov, O. A., Izmaylov, A. F. & Scuseria, G. E. Influence of the exchange screening parameter on the performance of screened hybrid functionals. *J. Chem. Phys.* **125**, 224106 (2006).
9   Xia, S. J. & Birss, V. I. A multi-technique study of compact and hydrous Au oxide growth in 0.1 M sulfuric acid solutions. *J. Electroanal. Chem.* **500**, 562-573 (2001).
10   Krempl, K. *et al.* Dynamic Interfacial Reaction Rates from Electrochemistry–Mass Spectrometry. *Anal. Chem.* **93**, 7022-7028 (2021).
11   Scott, S. B., Kibsgaard, J., Vesborg, P. C. & Chorkendorff, I. Tracking oxygen atoms in electrochemical CO oxidation-Part II: Lattice oxygen reactivity in oxides of Pt and Ir. *Electrochim. Acta* **374**, 137844 (2021).
12   Scott, S. B. Isotope-Labeling Studies in Electrocatalysis for Renewable Energy Conversion. *Ph.D. thesis* (2019).
13   Man, I. C. *et al.* Universality in oxygen evolution electrocatalysis on oxide surfaces. *ChemCatChem* **3**, 1159-1165 (2011).
14   Montoya, J. H., Garcia-Mota, M., Nørskov, J. K. & Vojvodic, A. Theoretical evaluation of the surface electrochemistry of perovskites with promising photon absorption properties for solar water splitting. *Phys. Chem. Chem. Phys.* **17**, 2634-2640 (2015).
15   Seitz, L. C. *et al.* A highly active and stable $IrO_x/SrIrO_3$ catalyst for the oxygen evolution reaction. *Science* **353**, 1011-1014 (2016).
16   Kim, D., Shi, J. & Liu, Y. Substantial impact of charge on electrochemical reactions of two-dimensional materials. *J. Am. Chem. Soc.* **140**, 9127-9131 (2018).
17   Zhao, X. & Liu, Y. Unveiling the active structure of single nickel atom catalysis: Critical roles of charge capacity and hydrogen bonding. *J. Am. Chem. Soc.* **142**, 5773-5777 (2020).
18   Nong, H. N. *et al.* Key role of chemistry versus bias in electrocatalytic oxygen evolution. *Nature* **587**, 408-413 (2020).
19   Bisbo, M. K. & Hammer, B. Efficient global structure optimization with a machine-learned surrogate model. *Phys. Rev. Lett.* **124**, 086102 (2020).
20   Larsen, A. H., Vanin, M., Mortensen, J. J., Thygesen, K. S. & Jacobsen, K. W. Localized atomic basis set in the projector augmented wave method. *Phys. Rev. B* **80**, 195112 (2009).
21   Larsen, A. H. *et al.* The atomic simulation environment-a Python library for working with atoms. *J. Condens. Matter Phys.* **29**, 273002 (2017).
22   Blum, V. *et al.* Ab initio molecular simulations with numeric atom-centered orbitals. *Comput. Phys. Commun.* **180**, 2175-2196 (2009).

23   Faas, S., Snijders, J. G., van Lenthe, J. H., van Lenthe, E. & Baerends, E. J. The ZORA formalism applied to the Dirac-Fock equation. *Chem. Phys. Lett.* **246**, 632-640 (1995).